A search for HVS candidates via simulation of trajectories

Bachelorarbeit aus der Physik

vorgelegt von

Simon Kreuzer

17.09.2013

Dr. Remeis Sternwarte Bamberg
Friedrich-Alexander-Universität Erlangen-Nürnberg

Betreuer: Prof. Dr. Ulrich Heber & Dipl. Phys. Eva Ziegerer

Contents

Abstract

Blue, massive stars are a puzzling feature of the Galactic halo. Such stars need dense gas and dust clouds to form, which are mostly found in the Galactic disk along the spiral arms. Assuming these locations as the birthplaces of massive halo stars, they need high velocities to reach their present-day position in the halo within their relatively short lifetime. Therefore, it is not surprising that halo objects showing high radial velocities were found in the past. The observed velocities of a couple of objects even exceed the Galactic escape velocity. Therefore, the stars are unbound to the Galaxy. Since now, most of these so called hypervelocity stars were found because of their high radial velocities. This work studies a different approach. It is about finding new hypervelocity stars to increase the available sample. The focus lies on estimating the full 6D phase space information for a sample of blue-type halo stars using simulations of their trajectories. Kinematic studies of the so called hypervelocity stars are able to provide further information about the mass and especially the shape of the dark matter halo of our Galaxy.

1. Introduction

Young, massive stars in the Milky Way halo are a puzzling fact. Such stars need dense gas and dust clouds to form, which are not present in the Galactic halo at all. Hence, young stars are mostly found in or near star forming regions in the Galactic disk - especially in the Galactic spiral arms. Therefore, it is assumed that young stars in the halo have been formed in the disk and were ejected from their place of birth. Due to the short lifetime of massive stars they need high velocities to reach their present-day position within their life period. Thus, they must be accelerated to very high velocities which can even exceed the escape velocity of the Galaxy. Accordingly, it is not surprising that some of these objects show high radial velocities. This bachelor thesis is about finding new candidates of high velocity stars in the Galactic halo.

1.1. Hypervelocity stars

Hills (1988) showed by numerical simulations that a binary, which comes close to the supermassive black hole in the Galactic center, might be disrupted (see Sec. 1.2.1). One star is captured in a close orbit around the black hole, while its former companion is ejected at a high velocity, which can even exceed the Galactic escape velocity. The ejected star is called *hypervelocity star* (HVS) (Brown et al., 2005). Brown et al. (2007) determined that 50% of these stars are expected to be unbound to the Galaxy and introduced the so called *bound hypervelocity stars* with expected Galactic rest-frame velocities between 275 km s^{-1} and 400 km s^{-1}. Meanwhile, also other possible mechanisms to accelerate stars to high velocities are known (see Sec. 1.2). The term HVS is in this thesis used for stars, travelling with high Galactic rest-frame velocities, and not only for stars which are unbound to the Milky Way.

The first HVS (SDSS J090745.0+024507) was discovered by Brown et al. (2005) with a Galactic rest-frame velocity of 709 km s^{-1}. It is called HVS 1 - most HVS discovered thereafter were numbered consecutively. The star is a 3 M$_\odot$ main sequence star. Hence, its distance to the Sun could be determined to be 110 kpc.

Just a few months later two more HVS were discovered by Hirsch et al. (2005) (US 708, HVS 2) and Edelmann et al. (2005) (HE 0437-5439, HVS 3), respectively. US 708 shows a radial motion of 708 $\pm$ 15 km s^{-1} in the Galactic rest-frame at a heliocentric distance of 19 kpc. It could be associated to the class of He-sdO stars, which are fainter than normal O-Stars. HE 0437-5439 is a normal B-type star at a heliocentric distance of 61 kpc, moving with a radial velocity of 563 $\pm$ 3 km s^{-1} in the Galactic rest-frame. The time of flight from the Galactic center to the present position exceeds the evolutionary lifetime for HVS 3. An attempt to explain the observations is, that it could be the merger of two lower-mass stars. A so-called *blue straggler* looks like a newly formed main sequence star with the total mass of a former binary.

Gualandris & Portegies Zwart (2007) concluded that, due to its distance of 19 kpc to the lage Magellanic cloud, which was determined by Edelmann et al. (2005), HVS 3 could have been ejected there with a velocity of about 500 km s^{-1}. They used a scenario which explains the present-day position of the star by dynamical ejection from a dense star cluster. Thus, the star would be able to reach its present position from the large Magellanic cloud rather than from the Galactic disk within its main sequence lifetime, without considering the merger scenario.

Targeted searches for HVS lead to the discovery of new stars travelling with high Galactic rest-frame velocities. Meanwhile, the catalogue published by Brown et al. (2012) consists of 39 HVS, 16 of them are unbound to the Galaxy.

One of the most promising aspects in studying HVS is, that they could provide further information about the central parsecs of our Galaxy - especially about the supermassive black hole. For example, if there were a binary black hole in the center of our Galaxy, the HVS should be found in a circle on the sky, because they should be ejected in a preferred plane. Furthermore, HVS offer kinematic data on larger distance scales than the Galactic disk. A statistical analysis could provide a way to fit the mass of the Milky Way to the kinematic data of the HVS. Additionally, the mass and especially the shape of the unknown dark matter halo could be determined. In order to do such an

analysis, a significant sample of HVS is needed and the open question about their origin has to be solved (see Sec. 1.2).

1.2. Possible origins of HVS and theoretical estimates

1.2.1. Hill's capture mechanism

In the late 80s Hills (1988) proposed the existence of HVS ejected from the Galactic center being an indirect evidence for a supermassive central black hole . If a close binary system approaches the Galactic center, it might be disrupted in 50% of all cases by the effect of tidal forces of the supermassive black hole. One member of the binary is captured in a close orbit around the central black hole. It is thought, that the central S-Star cluster, an accumulation of B-Stars in the central 0.04 pc, consists of such captured stars (Genzel et al., 2010). This hypothesis was recently tested and confirmed by Zhang et al. (2013) using numerical simulations. The binary companion star is ejected at very high velocities. The velocity at the time of ejection is, according to Genzel et al. (2010), given by

$$v_{HVS} = \frac{1.4 M_\bullet}{a_{12} \left(\frac{M_\bullet}{M_{12}} \right)^{2/3}} \tag{1}$$

where $M_\bullet = 4.2 \cdot 10^6$ M$_\odot$ (Schödel, 2011) is the mass of the central black hole, M_{12} the sum of the mass of both binary components and a_{12} its semi-major axis before disruption. Considering a semi-major axis in the order of 0.01 AU, which is common for binaries, the velocity at the time of ejection can be as high as 4000 km s^{-1}. This slingshot mechanism has been readily accepted as the most likely HVS accelerator, because other mechanisms seemed implausible. However, other mechanisms need to be considered as well.

Yu & Tremaine (2003) studied the production of HVS in more detail. They calculated estimated production rates for stars ejected at $v > 10^3$ km s^{-1}, but not only the mechanism proposed by Hills (1988) was taken into account. A close encounter of two single stars can also produce HVS. All prodcution rates, however, are low. Their estimates are summarized in Tab. Hills (1988). Nevertheless, a slingshot mechanism seems to be a promising scenario. A binary black hole in the center of the Galaxy can expel HVS in single star interactions at ten times higher rates. This would, according to Yu & Tremaine (2003), result in $\sim 10^3$ HVS within the solar radius of ~ 8 kpc. Indeed, it indicates that HVS are accelerated in the Galactic center, but, considering the incredible high number of 200 billion stars in the entire Milky Way, the given data also shows that HVS are a very rare phenomena. Therefore, only a few HVS were discovered yet.

close encounter of two single stars	$\sim 10^{-11} yr^{-1}$
hills mechanism	$\sim 10^{-5} yr^{-1}$
binary black hole - single star interaction	$\sim 10^{-4} yr^{-1}$

Table 1: Estimated production rates of hypervelocity stars in different mechanisms, calculated in numerical simulations by Yu & Tremaine (2003).

1.2.2. Disruption of satellite galaxies

A good knowledge of the full 6D kinematic data is necessary to calculate the trajectory of a star and therefore determine its origin. Having an adequate knowledge of this data, some HVS could not be traced back to the Galactic center, which implies that other mechanisms need to be considered as well. In contrast to the slingshot mechanism, Abadi et al. (2009) proposed, that HVS could also have been accelerated due to tidal disruption of dwarf galaxies by tidal forces of the Galaxy. A major amount of HVS in the currently known sample is located in the constellation of Leo. The observed velocities of these stars are lower than average. This can be a direct evidence for this scenario. A dwarf galaxy might has been disrupted in that area during the last 100 million years.

1.2.3. Binary supernova ejection

Irrgang et al. (2010) analyzed HIP 60350 ($v_{grf} = 530 \pm 35$ km s^{-1}) in detail and concluded, that it was ejected in the Galactic disk with a distance of 6 ± 0.6 kpc to the Galactic center. An origin in the center can therefore be ruled out. For instance, a star can be accelerated to this velocity by tidal interactions in a star cluster. Another promising scenario is, that a former binary companion of HIP 60350 was a massive star which died in a supernova. HIP 60350 would now be travelling with a major amount of its former orbital velocity in the binary. An evidence for this hypothesis are over-abundances of α-element lines found in the spectrum of the star, which are evidence for a nearby supernova. A similar scenario can be applied to HD 271791 (Heber et al., 2008). Both are HVS with extreme velocities which exceed the local escape velocity. Geier et al. (2013) were even able to apply this scenario to US 708 and found a possible progenitor system CD-30°11223, which may undergo the same process in the future. These outcomes challenge the scenario proposed by Hills (1988) as the only mechanism to produce HVS.

1.3. Stellar evolution

Analyzing stars in any way requires knowledge about their evolutionary processes, from their formation to their death. To initiate star formation a cloud, which consists of interstellar gas, has to undergo a collapse due to an increase of density. This collapse is mostly triggered by supernova shocks or density waves in the interstellar medium. The Jeans criterion gives a mass limit M_J in a certain volume at which the cloud becomes unstable against gravitational collapse.

$$M_J \sim \left(\frac{1}{\mu}\right)^{3/2} \left(\frac{1}{\rho}\right)^{1/2} \qquad (2)$$

where μ is the mass per particle and ρ is the density. For $M_{cloud} > M_J$ gravitational collapse occurs.

As the density in the cores of the formed clumps of interstellar gas increases, hydrogen fusion is initiated. A new star is born on the *main sequence* (MS) in the Hertzsprung-Russel-diagram (HRD) (see Fig. 1). In the HRD the luminosity L and absolute magnitude M_v of the stars, respectively, is plotted against effective temperature T_{eff} which is divided in spectral classes. The MS extends from the upper left to the lower right. It shapes the area in which central hydrogen fusion is the only source used for energy production. Our Sun is in this state of stellar evolution. The luminosity L and the lifetime on the MS τ_{MS} as well as further stellar evolution processes are sensitively predetermined by the initial mass, roughly as

$$L \sim M^{3.5} \qquad \tau_{MS} \sim 10^{10} \left(\frac{M_\odot}{M}\right)^{2.5} \quad (3)$$
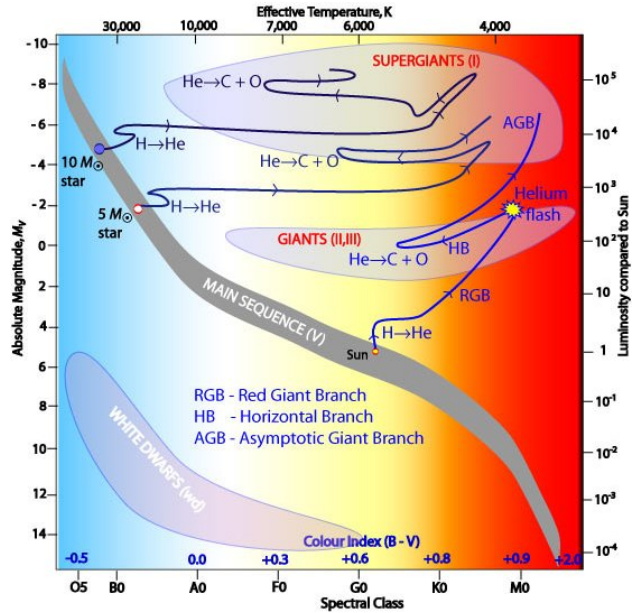
Figure 1: Hertzsprung-Russel-diagram (HRD) with post main sequence evolutionary tracks for selected stellar masses[1].

According to Eq. 3, stars with higher masses are much more luminous and burn their hydrogen fuel faster. In the HRD they are located on the upper part of the MS. While burning hydrogen, the star produces helium which is accumulated in the core. Therefore, the density in the core increases

---

[1]http://outreach.atnf.csiro.au/education/senior/astrophysics/stellarevolution_postmain.html

with time. For low mass stars ($M < 2.2$ M$_\odot$) the helium core becomes electron degenerate, which means, that there is no dependency between temperature and pressure any more. As the core becomes more massive, heating by the H-burning shell starts helium fusion suddenly. This process is called *helium flash*. For stars with initial masses higher than 2.2 M$_\odot$, helium fusion sets in an ideal gas situation. Therefore a flash does not appear.

Stars which are burning helium in the core are in the HRD located on the so-called *horizontal branch* (HB). It is called HB due to the almost horizontal position in the HRD. Accompanied by heavy mass loss to the interstellar medium, all stars on the HB have approximately the same mass ($\sim$ 0.5-0.6 M$_\odot$). But the position on the HB is again sensitively dependent on the mass and the metallicity of the star. More massive stars form the so-called *red clump*, which is located on the Red Giant Branch in the HRD. During this phase, the HE-burning shell is surrounded by an H-burning shell. In the core carbon, the ashes of the HE-burning shell, is accumulated. The star is (in the considered range of stellar masses) not able to burn carbon due to a lack of gravitational energy. As all helium fuel is burned, the star can not produce energy any more. The star becomes a cooling corpse, called a *white dwarf*.

Note, that stellar evolution of stars with $M > 8$ M$_\odot$ is not described, because it is not important for this work.

The evolutionary process of stars needs to be considered while determining the distance of an object (see Sec. 2.1.2). Uncertainties in stellar evolution processes lead to systematic errors in the distance determination and therefore to errors in the calculated trajectories. Especially because the MS is intersected by the HB, an association to a specific stellar population might be difficult in some cases. However, most HVS found were assigned to the MS.

Due to the age of the different stars, and therefore other metallicities, the population can furthermore be divided into two main groups:

- *Population 1*: Young stars, mainly found in the disk, especially in the spiral arms. They consist of reproduced material and therefore have an higher metallicity level, e.g. the Sun

- *Population 2*: Older stars, with somewhat lower metallicity level, e.g. halo stars.

1.4. The Milky Way gravitational potential

Calculating orbits requires an appropriate potential model of the Galaxy. Especially the dark matter halo affects stellar trajectories significantly. There are two requirements the potential model has to deal with:

- *Simple analytical potential*: A simple and analytical model is required to be capable to calculate many orbits in a short period of time.

- *Well fitted to observations*: A plausible model has to meet all observational constraints

Both is fulfilled by the potential of Allen & Santillan (1991), which has recently been updated by Irrgang et al. (2013). The Galactic potential is split into three parts, describing the bulge (Eq. 4), the disk (Eq. 5) and the dark matter halo (Eq. 6), respectively:

$$\Phi_{bulge} = -\frac{M_b}{\sqrt{R^2 + b_b^2}} \tag{4}$$

$$\Phi_{disk} = -\frac{M_d}{\sqrt{r^2 + \left(a_d + \sqrt{z^2 + b_a^2}\right)^2}} \tag{5}$$

$$\Phi_{dm} = \begin{cases} \frac{M_h}{a_h}\left(\frac{1}{(\gamma-1)}ln\left(\frac{1+\left(\frac{R}{a_h}\right)^{\gamma-1}}{1+\left(\frac{\Lambda}{a_h}\right)^{\gamma-1}}\right) - \frac{\left(\frac{\Lambda}{a_h}\right)^{\gamma-1}}{1+\left(\frac{\Lambda}{a_h}\right)^{\gamma-1}}\right) & \text{if } R < \Lambda \\[20pt] -\frac{M_h}{R}\frac{\left(\frac{\Lambda}{a_h}\right)^{\gamma}}{1+\left(\frac{\Lambda}{a_h}\right)^{\gamma-1}} & \text{otherwise} \end{cases} \tag{6}$$

In the equations given, M_i is the contribution of component i to the total potential, a_j, b_j are
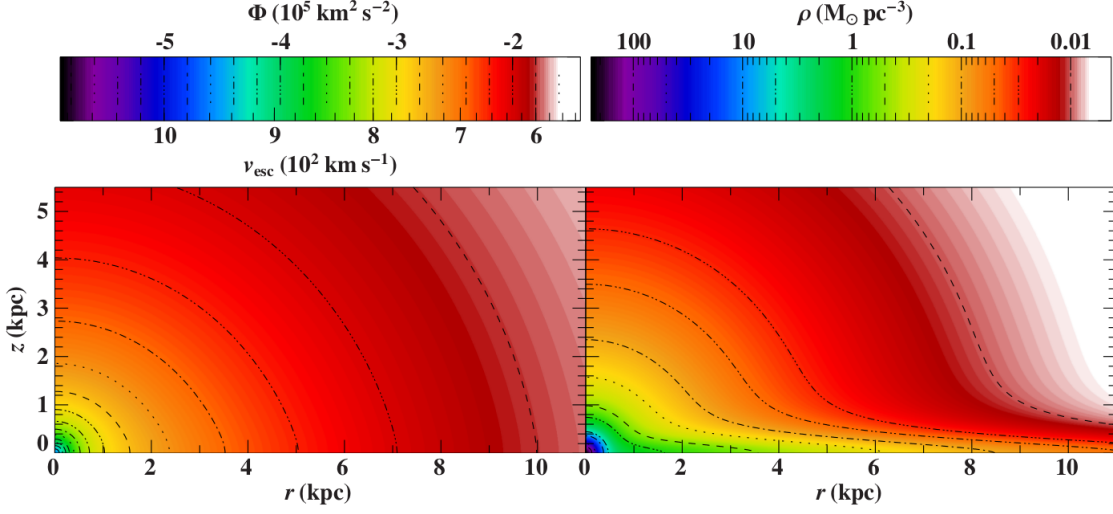

Figure 2: Edge-on view of the Milky Way potential and local escape velocity (left) and the fitted mass density (right). The disc is located at z=0. Adapted from Irrgang et al. (2013).

scale lengths. The parameter γ has been fitted to observations by Irrgang et al. (2013) and Λ is a cutoff parameter to prevent the dark matter halo from having infinite mass. This would be unphysical. Irrgang et al. (2013) fitted the potential to the rotation curve and used J1539+0239 as a test particle, which has to be bound to the Milky Way despite its negative amount of radial velocity, which results in $v_{grf} = 694^{+300}_{-221}$ km s^{-1}. As a result, the mass of the dark matter halo was underestimated in previous fits and the model is now fully consistent with all observations. Within a sphere with a radius of 100 kpc around the Galactic center, 96% of the total mass is found in the dark matter halo. Therefore, the halo is dominating the Galactic potential. An edge-on view of the potential and the fitted mass density can be seen in Fig. 2.

This potential was implemented as an isis-script (S-Lang based scripting language), which is used for all orbit calculations in this thesis. An adaptive Runge-Kutta algorithm of fourth/fifth order is used to integrate the equations of motion (see Sec. 2.2.1). The script is named "orbit calculator" in the following sections. In addition to the Galactic potential model described above, two other models can also be used. The main difference between them is the shape of the dark matter halo. A comparison of these potential models is given in Sec. 4.3. All potential models used were described in detail by Irrgang et al. (2013).

1.5. SDSS und Hyper-MUCHFUSS

All observational data used for simulations in this work are provided by the Sloan Digital Sky Survey (SDSS). Therefore a brief overview of this sky survey is presented in this section. The Hyper-MUCHFUSS project is a good example of what can be done with the SDSS data.

1.5.1. SDSS

The Sloan Digital Sky Survey (SDSS) is a fully automated survey of major parts of the sky visible from the northern hemisphere. As primary goal, redshifts of galaxies and quasars are measured. A 2.5m telescope at the Apache Point observatory in New Mexico, USA is used. The data is published in consecutively numbered data releases. In this work, data release 9 is used. The survey images the sky in five photometric bands ($u'g'r'i'z'$). In addition, a multi-fibre spectrograph is used to take 640 spectra per field for preselected stars. The objects to be spectroscopically analyzed are chosen by an algorithm which in the early days prefered, according to the original goals of the

project, galaxies and quasars. Nevertheless, especially blue stars are often misinterpreted, because they can look like quasars in photometry. Hence, there are spectra for many blue-type halo stars available in the database.

Data release 9 is the first data release, which includes data obtained by the new BOSS (Baryon Oscillation Spectroscopic Survey) spectrograph, but only about half of the survey area is already covered by BOSS. In addition, the current data release also contains data from the SDSS spectrograph, which was used for spectral analysis in previous data releases. Technical specifications of both spectrographs are compared in Tab. 2. Both spectrographs measured three spectra, each about 15 min exposure, for every object chosen by the algorithm. The spectra are mostly taken within the same night. Therefore, it is possible to detect rapid variations in radial velocity.

Feature	SDSS	BOSS
Fibers per plate	640	1,000
Fiber diameter	3 arcsec (180 μm)	2 arcsec (120 μm)
Wavelength coverage	3800-9200 Å	3650-10400 Å
Resolution	1500 at 3800 Å, 2500 at 9000 Å	
Wavelength calibration	< 5 km s^{-1}	

Table 2: Technical specifications of BOSS and SDSS spectrograph. BOSS is the next generation specrograph, used since data release 9. The resolution is given in $\frac{\lambda}{\Delta\lambda}$.[2]

Converting SDSS photometry ($u'g'r'$ $i'z'$ magnitudes) into the standard John-son-filter system is not straight-forward. A comparison of the two filter systems can be seen in Fig 3. In this work, just the apparent visual magnitude V is required for further analysis. According to Jester et al. (2005), this could be determined using the equation

$$V = g' - 0.59(g' - r') - 0.01. \quad (7)$$

1.5.2. Hyper-MUCHFUSS

The MUCHFUSS project (Massive Unseen Companions to Hot Faint Underluminous Stars from SDSS), initiated by Geier et al. (2011), made use of multiple-epoch spectroscopy pro-

Figure 3: Comparison between the normalised system respone in the $u'g'r'i'z'$-filter system (top) and the Johnson-filter system (bottom), adapted from Smith et al. (2002).

vided by SDSS and complemented them with additional spectra taken at 2-4 m class telescopes. They searched for hot subdwarfs with compact companions, and therefore high sinusoidal variations in radial velocity. The main target of that project were stars in the Milky Way halo. The companions were classified to be massive white dwarfs, neutron stars and black holes. As a side effect objects with a high but constant radial velocity were also found. These stars are possible HVS candidates. As a few of them were discovered during the project, the prefix "Hyper-" was added to the name of the MUCHFUSS project.

1.5.3. Collecting candidates

For this work, a list of appropriate and promising candidates was put together. Similar to MUCHFUSS, 100,000 candidates were preselected by color by Tillich et al. (2011) and spectra of
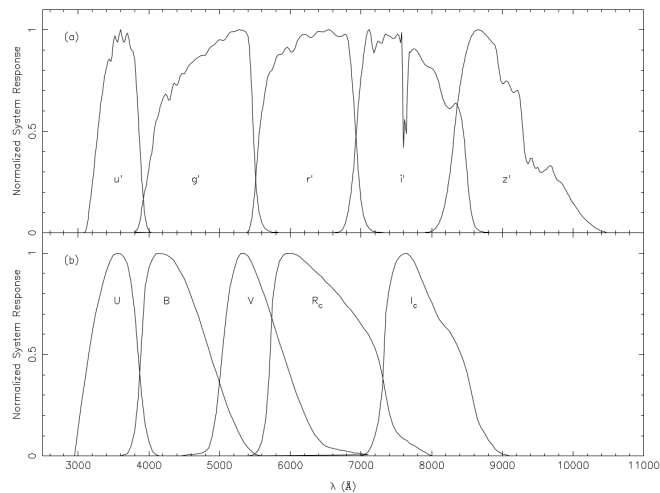
---

[2]http://www.sdss3.org/dr9/spectro/spectro_basics.php

stars of appropriate colors were extracted from the database if available. The selected objects are studied in this work. Furthermore, all objects Brown et al. (2012) studied were revisited. Other promising objects were contributed from different sources. The final sample contains 1300 blue-type halo stars. Indeed, all known HVS are blue-type stars. It is thought that the main reason for that is just a selection bias, because blue MS stars are very luminous and therefore visible over larger distance scales than redder objects. However, this type of stars is so numerous that it is difficult to find the very few HVS ones amongst them.

1.6. Kinematic approach

The proper motion describes the angular change of position of a star on the sky, the angular velocity in the two dimensional plane perpendicular to the line of sight, respectively. Brown et al. (2005) followed the idea of Hills (1988) and concluded, that a star at 50 kpc distance should have an expected proper motion of a few tenths of a milliarcsecond per year if it originates from the Galactic center. This value is small due to the large distance to the star, which leads to an expected low transversal velocity, since the Sun is just at ~ 8 kpc distance to the Galactic center. Most of the amount of the velocity should therefore be detected by measuring the radial velocity, which is the velocity in the line of sight. The radial velocity is easier to detect, as one only needs to determine the wavelength shift of spectral lines due to the Doppler effect in the spectrum of a star. To measure the proper motion, a sample of images of several epochs has to be analyzed by measuring the position of a star in comparison to background galaxies. In order to obtain the full 6D phase space information one has to measure the radial velocity, the proper motion, and the distance to the star, in addition to the given coordinates. As the proper motion is an angular velocity one has to know the accurate distance to the star to determine its real space velocity in the Galactic rest-frame v_{grf}. This velocity is defined according to Eq. 19. Most of the known HVS were found based on their high radial velocity. Proper motion values are mostly not known well enough to make statements about the real velocity of the star.

This bachelor thesis follows a different approach: The idea is to study halo objects and estimate their full 6D phase space information under the assumption that the star was accelerated in the Galactic center. Hence, stars with low radial velocity but high proper motion, and therefore a high Galactic rest-frame velocity could be found. Photometric methods were applied to estimate the distance and therefore determine the position of the star. To make estimations for the expected proper motion under the assumption that the object originates from the Galactic center, it was tracked back to the Galactic center in numerical simulations, in which the proper motion was a free parameter. A list of 1300 appropriate halo objects, provided by Tillich, Ziegerer and Scholz, was analyzed in these kinematic simulations to obtain a priority list. Knowing the expected proper motion of a star, one can determine its expected Galactic rest-frame velocity. The goal is to obtain a sample of the objects which show the highest expected Galactic rest-frame velocity and measure the proper motion of two of them.

2. Tracking Orbits

2.1. List of Objects

To be able to calculate orbits and track stars back to the Galactic center, the whole information about the 6D phase space motion is needed. Beginning with the coordinates and radial velocities of all objects, this and the following sections aim at estimating the distance, such that 3 space coordinates and the radial velocity are known. Thus, an object is be fixed in 4 dimensions of its phase space. Just the velocity in the plane perpendicular to the line of sight - which causes the proper motion - remains unknown. It is assumed that the candidates originate from the Galactic center and the proper motion components (μ_α, μ_δ) are free paramters to be fitted by trajectory calculations.

2.1.1. Retrieving Data from SDSS DR9

To extract data from the SDSS DR9 database, the SDSS CasJobs interface, a web interface for SQL-queries in the SDSS database, is used[3]. For further processing, the existing sample has to be matched with the database to obtain the coordinates with high precision. Additionally, the visual magnitude of each object needs to be calculated from the u'g'r'i'z' magitudes (See Sec. 1.5.1) to estimate its distance (see Sec. 2.1.2) and stellar parameters (see Sec. 2.1.3).

Only coordinates and radial velocities of all 1300 objects were known, thus no general identifier exists. In addition, SDSS could have recognised a star at a slightly different position, than the known coordinates. Therefore an SQL script was written, which searches for objects within a circle with radius 1 arcsec around the known coordinates. The value of 1 arcsec was chosen after many test runs. It is limited due to the requirements, that on the one hand no other objects should be in the search field, which can lead to wrong matching, and on the other hand the object itself has to be recognised by SDSS within the selected search field. The resulting list of SDSS-coordinates and the u'g'r'i'z' magnitudes was used for the kinematic analysis of all objects.

2.1.2. Distance determination

To obtain the full 3D position vector

$$\vec{x} = d \begin{pmatrix} cos\theta cos\phi \\ cos\theta sin\phi \\ sin\theta \end{pmatrix} \tag{8}$$

of an object, one needs to determine the distance d. Here, θ and ϕ are measured in a Galactic spherical coordinate system with the Galactic center at the origin. To calculate the distance analytically, consider a star with radius r and integrated flux F through its surface observed at a distance d. F gives the power of radiation per area, hence the dimension is W m^{-2}. Ignoring interstellar extinction, one can write the equation

$$\oint F = \oint f \tag{9}$$

$$4\pi r^2 F = 4\pi d^2 f \tag{10}$$

where f is the the integrated flux through a spherical surface at distance d. Hence, measuring the flux f on a certain surface at distance d and knowing the flux F at the surface of the star, it is possible to determine the distance to the object:

$$d = \sqrt{\frac{r^2 F}{f}} \tag{11}$$

---

[3]http://skyserver.sdss3.org/casjobs

The unknown radius of the star can be determined using Newtons gravity law. Therefore,

$$g = \frac{GM}{r^2} \quad \Rightarrow \quad r^2 = \frac{GM}{g} = \frac{GM}{10^{\log\ g}} \tag{12}$$

where G is the gravitational constant, M is the mass of the star and g its surface gravity. The flux is normalised to 10pc distance to the star.

$$F(10pc) = \frac{r^2}{10pc} \cdot F \tag{13}$$

The normalised flux can be used to determine the absolute magnitude M_v of the star.

$$M_v = -2.5 \log \frac{F(10pc)}{0.358} \tag{14}$$

The constant in the denominator is a historical remnant due to calibration of the magnitude scale. Note, that the absolute magnitude is an indicator for the observed luminosity at a distance of 10 pc. Considering the distance modulus

$$m - M_v = -2.5 \log d - 5 \tag{15}$$

, where d is measured in units of 10 pc, the distance of a star can be determined using the equation

$$d = 10^{\left(\frac{m-M_v}{5} - 1\right)} \tag{16}$$

The main problem concerning this approach is, that the flux through the star's surface is unknown. Therefore, the flux was determined by a linear interpolation of model grids for stellar atmospheres computed by Kurucz (1992). Since the flux is a function of the effective Temperature T_{eff} and the surface gravity $\log g$, both values need to be known. They can be determined using spectra.

2.1.3. Parameters of stellar atmospheres

Atmospheric parameters need to be derived from spectra. Comparing the resulting expected absolute magnitudes of the spectral analysis to the observed m_v provides best information about the distance to a star. However, this procedure will not be applied in this work, because the spectral analysis of all 1300 candidates would be a time-consuming job. Therefore, a photometric distance estimation is preferred for its simplicity.

The first step in estimating the distance was to derive certain stellar parameters, like the effective temperature T_{eff}, the Mass M and the gravity on the surface of the star $\log g$. All parameters have to be estimated out of the magnitudes measured by SDSS. These parameters were used for estimating the distance to each object as described in Sec. 2.1.2.

Converting SDSS photometry into the visual magnitude (Johnson-filter) At the beginning, $u'g'r'i'z'$ magnitudes were converted into the standard Johnson system. Therefore Eq. 7 was applied to the data. The error was estimated using standard error propagation.

$$\Delta V = 0.41 \Delta g' + 0.59 \Delta r' \tag{17}$$

Mass determination and evolutionary status In the sample of 1300 blue stars, it is not always clear whether an object is a MS star or a star on the HB, because both objects have similar colors. For instance, MS stars with masses of 3 to 5 $M_\odot$ are located in the same region of the HRD and of the $\log T_{eff}$-$\log g$-diagram as HB stars. Evolutionary tracks for MS stars obtained by Schaller et al. (1992) are shown in Fig. 4. In addition, the ZAMS (zero age main sequence) is plotted which gives the positions of a newly formed star at the beginning of its MS evolution, depending on the mass. ZAHB (zero age horizontal branch) and the TAHB (terminal age horizontal branch) show
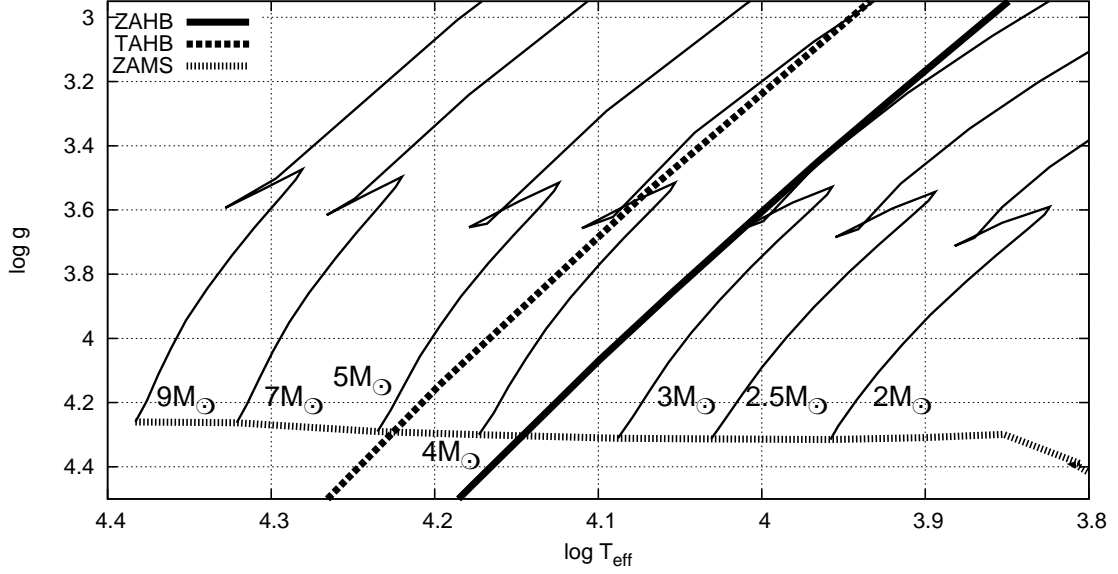
Figure 4: Evolutionary tracks for MS stars, derived by Schaller et al. (1992), and the pathway of ZAHB (Zero Age Horizontal Branch), TAHB (Terminal Age Horizontal Branch) and ZAMS (Zero Age Main Sequence), derived by Dorman et al. (1993).

the beginning and ending of the HB phase, respectively. The mass of MS and HB stars varies slowly with T_{eff}. It is sufficient to assume that all HB stars in the selected color range have the same mass of 0.55 M$_\odot$.

Stars with a certain apparent magnitude m_v that are located within the area where both, MS and HB option, is possible, are either distant - intrinsically bright - massive B-type stars or closer - intrinsically fainter - blue HB stars. The effective temperature and the surface gravity differ much between the two classes of stars, and both is additionally dependent on the mass of the star. This leads to different luminosities, and therefore different absolute magnitudes M_v. Note, that the absolute magnitude describes the luminosity at a distance of 10 pc. Considering the distance modulus

$$m_v - M_v = 5 \log d - 5 \tag{18}$$

where m_v is the apparent magnitude measured on earth and d is the distance in pc, an unknown absolute magnitude M_v leads to an uncertainty in the determined distance. Hence, at least two different cases need to be considered for every star. The star can either be a normal MS star or a star on the HB. Furthermore (as mentioned above) the stellar parameters even show major differences depending on the mass of the MS star. Hence, no scenario could be ruled out and every possible parameter setting (which can exist) was be taken into account for the moment. Even the trajectory was subsequently calculated for every possibility. In the following paragraphs, the process of obtaining the parameter configurations will be described in detail.

Estimating the temperature with color-color-diagrams
To divide the sample of objects into different temperature intervals, a color-color-diagram was applied. Fig. 5 shows
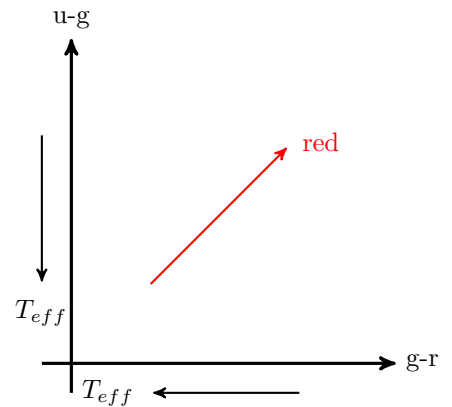

Figure 5: Schematic color-color-diagram, the effective temperature increases to the lower left corner, while the reddening vector points to the top right corner, according to Kim & Lee (2007).

the general idea. Magnitudes of two different filters are
subtracted. In this representation $u' - g'$ and $g' - r'$ is used. The resulting values are called *color indices* and plotted over each other. Color indices represent temperatures. Choosing the more blue filter to be subtracted from the more red one, which is done here, leads to higher effective temperatures in the lower left of the diagram. Furthermore, a so called *reddening vector* exists, which points to the upper right in the color constellation used in this work (Kim & Lee, 2007). The reddening vector shifts objects in the color-color-diagram to be more red, resulting in a general underestimation of the temperature. This effect is caused by interstellar extinction.

Castelli & Kurucz (2004) computed new grids of stellar model atmospheres, providing relations between stellar parameters, such as effective temperatures, gravity, and $u'g'r'i'z'$-magnitudes. To divide the sample of objects into appropriate temperature intervals of ~ 1000 K, the color indices of the sample are overplotted with the color indices obtained by Castelli & Kurucz (2004). The value of 1000 K was chosen, because this would lead to a typical error of 0.2 in log g. The values of each parameter configuration were obtained using the mentioned grids of stellar model atmospheres and the procedure described in Sec. 2.1.2. In Fig. 6 can be seen, that the plotted lines of constant log g roughly fits to the data, but determining the gravity from color indices is not possible because a large difference in log g has no significant difference in the color-color-diagram. In addition, possible values for log g at a constant temperature are plotted. They are used to intersect the sample of stars 'by eye' into different parts, depending on the temperature. It should be kept in mind, that the reddening is roughly unknown but small because of the high Galactic latitude. The effect of metallicity is ignored because it is estimated to be small against the errorbars.
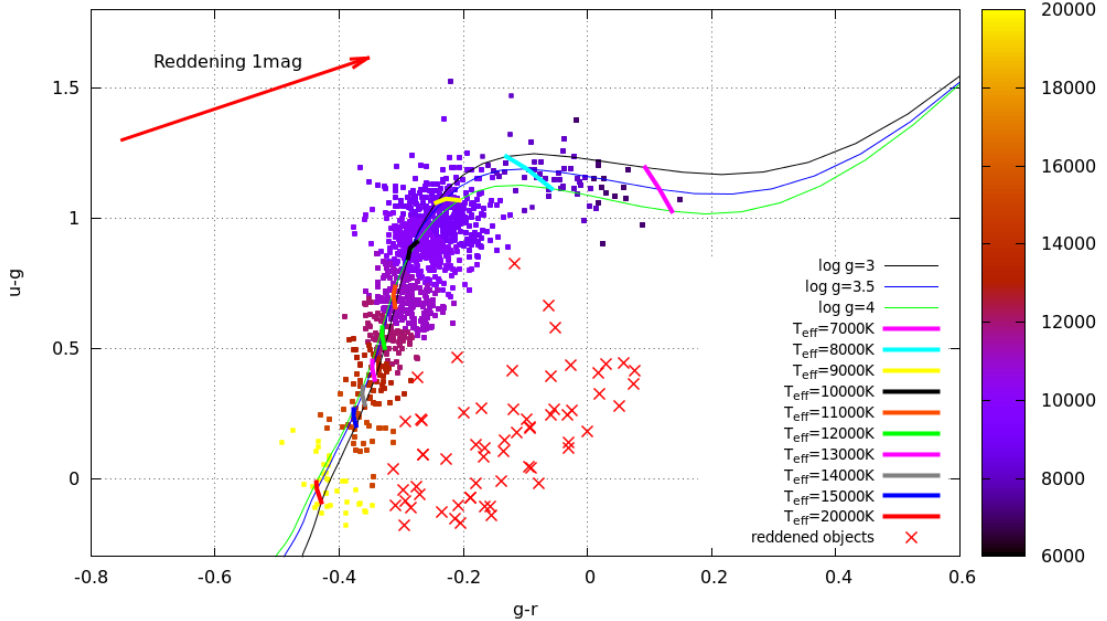

Figure 6: Color-color-diagram of the sample, over-plotted with lines of constant log g, and log g for constant temperature, according to Castelli & Kurucz (2004). The sample is divided 'by eye' into temperature intervals of 1000 K. The reddening vector corresponds to a reddening of 1 mag due to interstellar extinction, according to Kim & Lee (2007). Objects marked as red stars were ignored.

Objects on the lower right of the accumulation are either reddened very strong or are binary stars and therefore brighter than single stars. Thus, they could not have been associated to a fixed temperature and were therefore ignored. On the other hand, all objects too far away from the accumulation were ignored as well, despite they could be interesting objects, but single objects are not the main target of this work.

Other stellar parameters The sample was subsequently divided into parts with different effective temperatures. Every object was associated to a specific temperature interval. As mentioned above, it is also necessary to take the two possibilities of stellar evolutionary states (MS and HB) into account, and even consider different initial masses for MS objects. This could not be done using the color plot, due to different problems including the uncertainty in reddening and the error of the SDSS magnitudes. Spectra with appropriate resolution were not available for each object and therefore a precision check of these values was not possible. Therefore, every T_{eff} interval was furthermore divided into different cases. The MS case was divided into appropriate intervals between 2-9 $M_\odot$. For objects on the HB, three different evolutionary states were taken into account. The difference between the $\log g$ configuration of the star between ZAHB and TAHB is in the order of 0.4. The possible parameter configurations were obtained from the evolutionary tracks shown in Fig. 4 and are listed in Tab. 3. Parameter configurations which produce unrealistically large distances (>200 kpc) without exception were ruled out.

T_{eff}	log T	2M$_\odot$	2.5M$_\odot$	3M$_\odot$	4M$_\odot$	5M$_\odot$	7M$_\odot$	9M$_\odot$	ZAHB	TAHB	HB
7000	3.845	3.65	3.2	3.0	2.7	2.4	2.0		2.95	2.55	2.75
8000	3.903	3.95	3.55	3.2	2.85	2.6	1.95		3.15	2.8	2.98
9000	3.954	4.3	3.8	3.4	3.05				3.4	3.05	3.22
10000	4		4.1	3.75					3.6	3.25	3.43
11000	4.041			3.95	3.35				3.8	3.4	3.6
12000	4.079			4.25	3.6				4	3.6	3.8
13000	4.114				3.85	3.4		4.14	3.75	3.95	
14000	4.146				4.05	3.6	3.1	2.85	4.3	3.9	4.1
15000	4.176					3.7	3.25	2.95	4.45	4.05	4.25
20000	4.301						4.1	3.55			

Table 3: All $\log g$ configurations taken into account, determined from the evolutionary tracks shown in Fig. 4. For all HB cases 0.55 $M_\odot$ is assumed. The HB option was obtained in the middle between ZAHB and TAHB.

Resulting distances The described procedure was applied to the complete sample, to estimate the distance of each object. Furthermore, standard error propagation was applied. The errors on the effective temperature are estimated to be 1000 K at the 1 σ level. The errors on logarithmic surface gravity are estimated to be 0.5. Due to these errors, the mean relation between distance and its 1 σ value is $\left\langle \frac{\sigma}{d} \right\rangle = 0.133$.

2.2. Fitting Orbits

Four components of the 6D phase space were at this time known for every object in the sample - three components of the position and one component of the velocity vector. The missing information were the proper motion of the target. We shall assume that the stars originate from the Galactic center and compute the corresponding proper motion components. The aim of this section is, to estimate the proper motion of the star. For this purpose the orbit was calculated back in time, using the four known dimensions of the phase space. Subsequently, the proper motion values were varied using a χ^2-fit routine, so that the trajectory originates as close as possible is the Galactic center. The proper motion of two objects is measured in this work to check the approach. More results can be approved or disproved by future measurements.

2.2.1. Orbit calculation

To calculate trajectories in the potential of the Milky Way, the script *orbit calculator*, introduced in Sec. 1.4, and also the Galactic potential model introduced there was used. Calculating a trajectory in a potential means solving an ordinary differential equation (DE) of motion. To solve such

problems, many numerical algorithms exist. A simple and well tested DE solver is the adaptive Runge-Kutta algorithm, which is applied in the orbit calculator.

With initial conditions given, this algorithm computes the solution of the DE, starting with given initial values, step by step. To go to the next step in the solution space, four slightly different calculations of one step are done. Therefore the derivative is evaluated at 4 different points. The algorithm is designed in a way, that two of the four steps slightly overestimate the next value, while the two others slightly underestimate the next value. Thus, a good mean value can be determined by weighting each value appropriately. The difference between the four calculations is an indicator for the quality of the calculated step. If it exceeds a pre-chosen limit, the integration step was too big and the calculation has to be done again with a smaller step size. This limit can be adapted to the derivation of the trajectory in the previous step. Thus, if the trajectory changes very fast in direction, the algorithm will calculate smaller steps and therefore obtain the precision needed. The same mechanism can be applied to increase the step size, if the solution changes very slow. The algorithm is therefore able to adapt the step size, according to the rate of change in the computed solution. A few steps have to be computed twice or more times. However, an adaptive Runge-Kutta algorithm all in all saves much resources, but the precision remains at a high and constant level.[4]

As long as a star moves in the nearly devoid Galactic halo, the potential model of the Milky Way is expected to be able to produce realistic trajectories. But if the trajectory passes the Galactic disk of the Milky Way, other massive objects and especially clouds of interstellar gas and dust will influence the trajectory. Furthermore the inner structure of the Galactic disk e.g. the position and movement of spiral arms and open clusters needs to be considered in these cases, which lies beyond the scope of this work. The perturbers of the Galactic disk are complicated to derive due to turbulent and random interaction. Hence, every calculation is stopped, if an object reaches the Galactic disk within a radius of 15 kpc around the Galactic center. Furthermore, the calculation is also stopped, if the travel time exceeds 10 Gyr, to prevent the algorithm from integrating a trajectory to infinity, which might occur, if the calculated trajectory does not hit the Galactic disk in the past.

2.2.2. Fit-function

The next step is to fit the proper motion values in right ascension (μ_α) and declination (μ_δ) to generate a trajectory, which originates as close as possible to the Galactic center. As a criterion, the distance between the point of the trajectory, which has minimal distance to the Galactic center, and the Galactic center itself, is minimized.

To visualize the final results of this process a two dimensional *confidence map* from -10 to +10 mas yr^{-1} was generated first. The values for proper motion in right ascension and declination were divided in 80 steps each. For each combination an orbit was calculated and the minimal distance between trajectory and Galactic center was calculated. Two representative confidence maps are shown in Fig. 7. The complex structures, especially visible in the right-hand map, originates from the fact that the simulation was stopped, when the trajectory hits the Milky Way. In addition, the corresponding 'minimal' trajectories are also shown. Due to the high complexity the usage of a standard 'steepest descend' method to find the global minimum was ruled out before trying. Such algorithms are likely to converge into local minima. The minimum would therefore depend on the choice of the initial parameters.

If the confidence map is flat on a local scale and shows extended areas of constant distance from the Galactic center, a fit algorithm would try to vary the proper motion values, and conclude, that fitting is not possible, because the parameter to minimize (the minimal distance to the Galactic center) does not change. This is the case if the current position of a star is the point of the entire trajectory which is closest to the Galactic center. Furthermore, extended local minima can dominate the confidence map, which are mostly produced - as mentioned above - by the fact that the simulation is stopped, if the trajectory hits the Galactic disk. Some trials with a simplex algorithm, which could possibly deal with the local minima problem, also failed due to the large

---

[4]All informations about the Runge-Kutta algorithm adapted from Numerical Recipies, William H. Press, Cambridge University Press, 2007, Third Edition
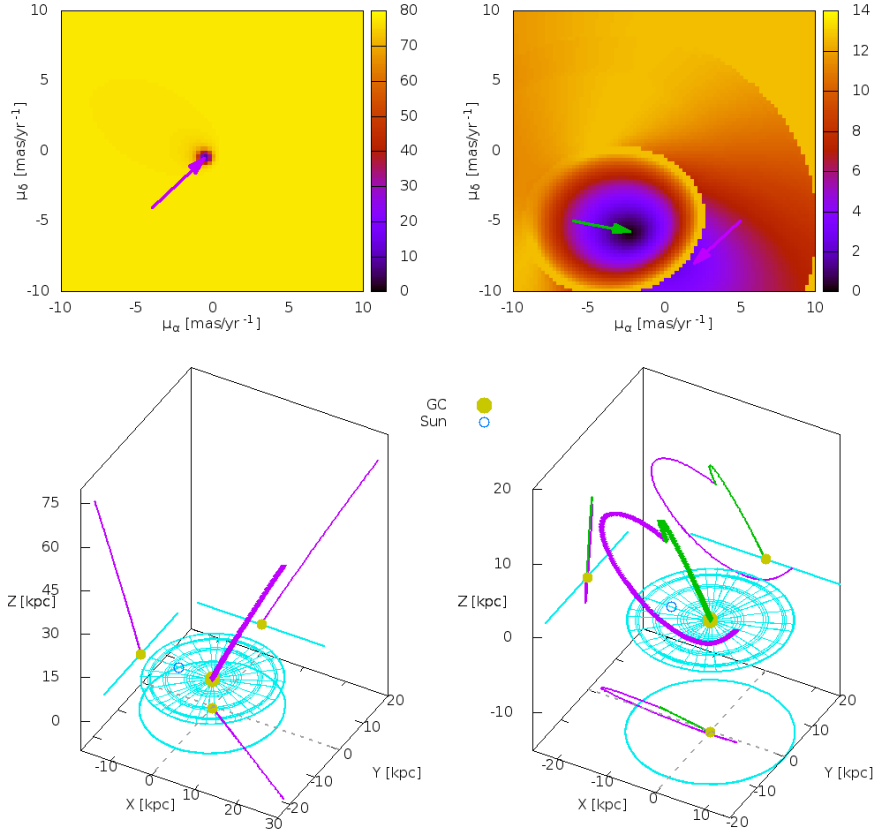
Figure 7: Top: Representative confidence maps for proper motion, showing a small minimum (left) and complex structures (right). The color indicates the minimal distance to the Galactic center in the entire trajectory. Bottom: Corresponding trajectories of selected points in the confidence map. The coloor of the arrow corresponds to the trajectory plotted in the same color. The Galacitc disk ($r = 15$kpc) and the positions of the Sun and the Galactic center are marked.

extent of the local minima. One way to solve the convergence problem could be to obtain better initial conditions for the fitting routine.

Therefore, a confidence map was needed for every object in the sample. Due to the sharp minima, it was not possible to get along with a lower resolution than shown above. The calculation of these 1300 confidence maps required large computational resources, because for all parameter configurations of an individual star, $80 \cdot 80 = 6400$ trajectories had to be calculated. Subsequently, the minimum of the confidence map could have been detected and its proper motion values was forwarded to the fitting routine as initial values. The position of the minimum was then approximately known. Hence, a convergence into another local minimum could be ruled out and a normal 'steepest descent' fitting algorithm could be applied.

Confidence map evolution due to different stellar parameter configurations   This procedure was applied to every possible parameter configuration taken into account (see Sec. 2.1.3). Therefore, the determined distance varies between the different possible options of each star - and therefore the confidence map changes. Fig. 8 shows the evolution of the confidence map for all different parameter configurations and corresponding distances. The 0.55 $M_\odot$-plots indicate the HB cases. Note the different color scale on each plot. If the object is at a lower distance the confidence map shows more structural complexity than at higher distances. This originates from the fact, that the proper motion is an angular velocity, and therefore, the space velocity increases with distance for a
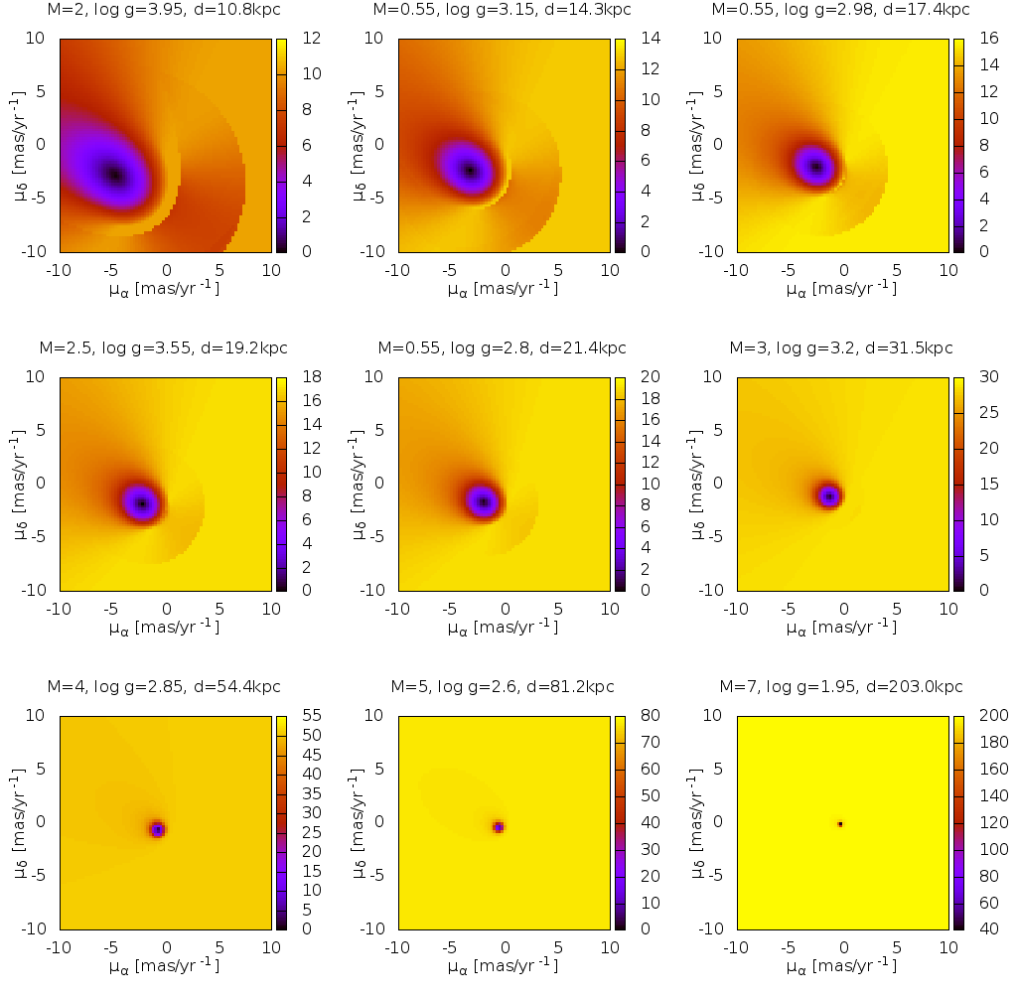
Figure 8: Confidence maps for all parameter configurations of candidate SDSSJ134851.56+001244.26. The color indicates the minimal distance between trajectory and Galactic center, plotted for values from -10 to 10 mas yr^{-1} of proper motion in both directions, right ascension and declination. The corresponding stellar mass, surface gravity and distance are given above each plot. The stellar mass is given in solar masses. The 0.55 M$_\odot$ options indicate the HB caseses of the star. the different color scale on each plot.

given proper motion. The small minima in the bottom row show again the need to calculate the confidence map in high resolution. In the lower right plot, the object is even too far away to resolve the small minimum in the confidence map. There, a minimal distance of (41.6 kpc) to the center is indicated, but the fit routine was able to find a trajectory which originates in the Galactic center.

2.3. Galactic rest-frame velocity and escape velocity

Another interesting question is, whether a star is bound or unbound to the Milky Way. This could be determined by comparing the Galactic rest-frame velocity v_{grf} and the local escape velocity v_{esc} at the star's position. If $v_{grf} > v_{esc}$, the star is unbound to the Galaxy.

Consider a euclidic, right handed coordinate system. Its origin is located in the Galactic center, the y-axis points in the direction of the Sun and the z-axis is perpendicular to the Galactic disk. As all dimensions of the phase space are known by now, the Galactic rest-frame velocity can be determined straightforwardly, using

$$v_{grf} = \sqrt{v_x^2 + v_y^2 + v_z^2} \tag{19}$$

To determine the local escape velocity, the potential Φ_{local} at the star's position was calculated. The criterion to be unbound was set to a star being able to travel more that 200 kpc away from the Galactic center with its own total energy.

$$E_{pot} + E_{kin} = E_{pot}(R = 200 \text{ kpc}) \tag{20}$$

Cancelling the test mass gives

$$\Phi(\vec{R}) + \frac{1}{2}v^2 = \Phi(R = 200 \text{ kpc}) \tag{21}$$

Since the potential model of the Milky Way is not spherically symmetric, $\Phi(R = 200\text{kpc})$ is depending on the direction. However, the difference between $\Phi(R = 200 \text{ kpc})$ in the x-y-plane and in z-direction is not very large. Thus, an average value is adopted. Resolving the equation for v gives an expression for the local escape velocity, with ξ being an optional constant to be able to obtain the correct units.

$$v_{esc} = \xi \cdot \sqrt{\Phi(R = 200\text{kpc}) - \Phi(\vec{R}) \cdot 2} \tag{22}$$

3. Results

3.1. Selecting promising objects

For every star of the 1300 targets, this procedure was carried out testing all combinations of parameters. After all simulations, a priority list was created. It consists of objects which were most promising to show high velocities and was used to help to decide which star's proper motion should be measured. The selected objects have to fulfil certain criteria. It is self-evidently that the most important criteria should be about velocity. Selected objects should show a high predicted v_{grf}. Additionally, the predicted proper motion should be sufficiently high to make measurements feasible. Therefore, objects with a high calculated value of proper motion are preferred. However, a high value of proper motion does not guarantee a high Galactic rest-frame velocity, which is another important criteria. Moreover, the option of being unbound to the Galaxy, which can be determined according to Sec. 2.3, maybe makes an object more interesting. In App. A an overview including the most interesting objects and their kinematic data is given. Note, that there is no intrinsic arrangement by priority in the list. Due to the different parameter configurations more than one possibility exists for each object. However, a combination of parameters which leads to a short heliocentric distance is often able to produce an easily measurable amount of proper motion. To select objects to be on the priority list, the following criteria were applied, in addition to the general criteria mentioned above.

- **Closest solution**: The solution with the shortest heliocentric distance is considered in the list. Some objects can be found in the list twice. These exceptions show different parameter configurations that lead to interesting values of proper motion and/or interesting trajectories.

- **Visibility**: A suitable set of information about a target (including a spectrum) requires good visibility of the object. Therefore, a bright m_v was preferred composing the priority list.

- **Comparing with spectra**: Choosing the parameter combination with the smallest heliocentric distance for further processing seems to be a decent choice, when comparing the temperature and log g data of the parameter combination to data obtained using SDSS spectra. The spectra were analyzed in a third party work by Eva Ziegerer by fitting model atmospheres to the spectra measured by SDSS. The moderate resolution of the SDSS spectra is sufficient to make good estimations. A comparison of assumed and derived parameter settings of the most promising candidates is also given in App. A in Tab. 10. Not for all promising candidates SDSS spectra were available.

3.2. Statistical analysis

A large sample of objects calls for applying the statistical toolbox. First, the distribution of the expected Galactic rest-frame velocity is studied in this chapter. Subsequently, the predicted proper motion values are compared to automatically measured values. These measurements were done by SDSS and PPMXL. Both provides a check for the quality of the approach of this work.

3.2.1. Distribution of v_{grf}

To study the results of all calculations, the Galactic rest-frame velocity v_{grf} was calculated for each star. A Gaussian distribution with its peak at about 200 km s^{-1} - typical v_{rot} of the Milky Way - is expected for halo stars, but not necessary. Stars ejected from the Galactic center can also produce other velocity distributions. Fig. 9 shows a histogram of the v_{grf} values determined for the (heliocentric) closest possible solution of each object. The fitted Gaussian distribution has its peak at 40.9 km s^{-1} which is much lower than expected. Analyzing this histogram by eye shows, that the peak consists of two different ones. The reason for this effect remains unclear. Some objects also show high v_{grf} up to 1000 km s^{-1}, but in some checks these objects are not promising to be existing HVS. The main reason for their high velocities is, that the solution with the shortest

distance is close to the Galactic disk and therefore the star needs very high velocities to have a trajectory with its origin in the Galactic center. Taking a solution into account, which is only a little bit more distant changes the expected v_{grf} to much lower values. Nevertheless, these stars could be interesting objects. However, neglecting these objects, most stars were predicted to be slower than typical halo stars.

In fact, stars ejected from the Galactic center with high velocities are expected to have highly elliptical orbits around the Galactic center and therefore small velocities near their apastron position. Most of the time these stars would stay at these large distances to the Galactic center, while the rest of the trajectory is covered in a relatively short period of time, due to Kepler's second law. This effect is indeed expected, because all trajectories were calculated under the assumption that the star originates in the Galactic center. All in all, the distribution of v_{grf} is plausible. In real measurements, the solution could be quite different. If the stars in fact were not ejected by the Galactic center but are 'normal' halo stars, the velocity distribution could be completely different than the distribution given in Fig. 9.
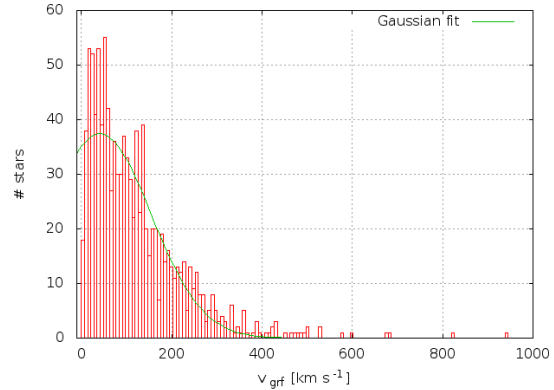

Figure 9: Calculated distribution of v_{grf}. The peak of the Gaussian fit is located at 40.9 km s^{-1} and its σ is 113.8 km s^{-1}. This peak is found at relatively low velocities. The histrogram shows some peaks at high velocities, but the corresponding objects were not promising to be existing HVS.

3.2.2. Comparing calculated proper motion with SDSS and PPMXL

SDSS and PPMXL[5] provide automated proper motion measurements, done with an algorithm. Comparing these measurements with the predicted values of this work can give further information about the worthiness of the approach. To visualise the results, the values obtained by SDSS and PPMXL were plotted over the predicted ones - calculated under the assumption that the star originates from the Galactic center. The resulting distribution can be seen in Fig. 10, plotted in right ascension and declination. Note, that the plotted difference is expected to follow the plotted line if both values correspond to each other. Stars which were not measured by SDSS or PPMXL yet, were thrown out. At first glance, the data seems not to fit to the predicted values. In general, the SDSS data seems to fit a bit better. However, large discrepancies and scattering of the data can be seen. The differences between the corresponding values are in the same order of magnitude than the values themselves. Therefore, the given distribution can indeed be interpreted as a random distribution. In general, the proper motion seems to be underestimated by the calculations. This causes the left-shift visible in all plots. Due to the large scattering, there is no direct evidence for the stars to originate in the Galactic center, but the assumption could also not be dis-proven: Indeed, a small amount of stars seem to follow the plotted line and therefore show the predicted proper motion.

Note, that it is very difficult to measure the proper motion of a body on large distance scales > 5 kpc. Sec. 4.2 shows again that the error bars are in the same order of magnitude than the values themselves - even in a not-automated measurement. Thus, even in between the data provided by PPMXL and SDSS a lack of consistency can be seen. A plot similar to Fig. 10 is given in the App. B to compare these sets of data. An estimation of the uncertainties is impossible without studying the algorithm and raw data used by SDSS and PPMXL. This would go beyond the scope of this work. The error bars provided by SDSS and PPMXL are of the order of 2-10 mas yr^{-1} and even do not overlap for some objects. This shows again that automated measured values should be taken with a grain of salt. All in all, the statement of the random distribution given above cannot be proven or dis-proven.
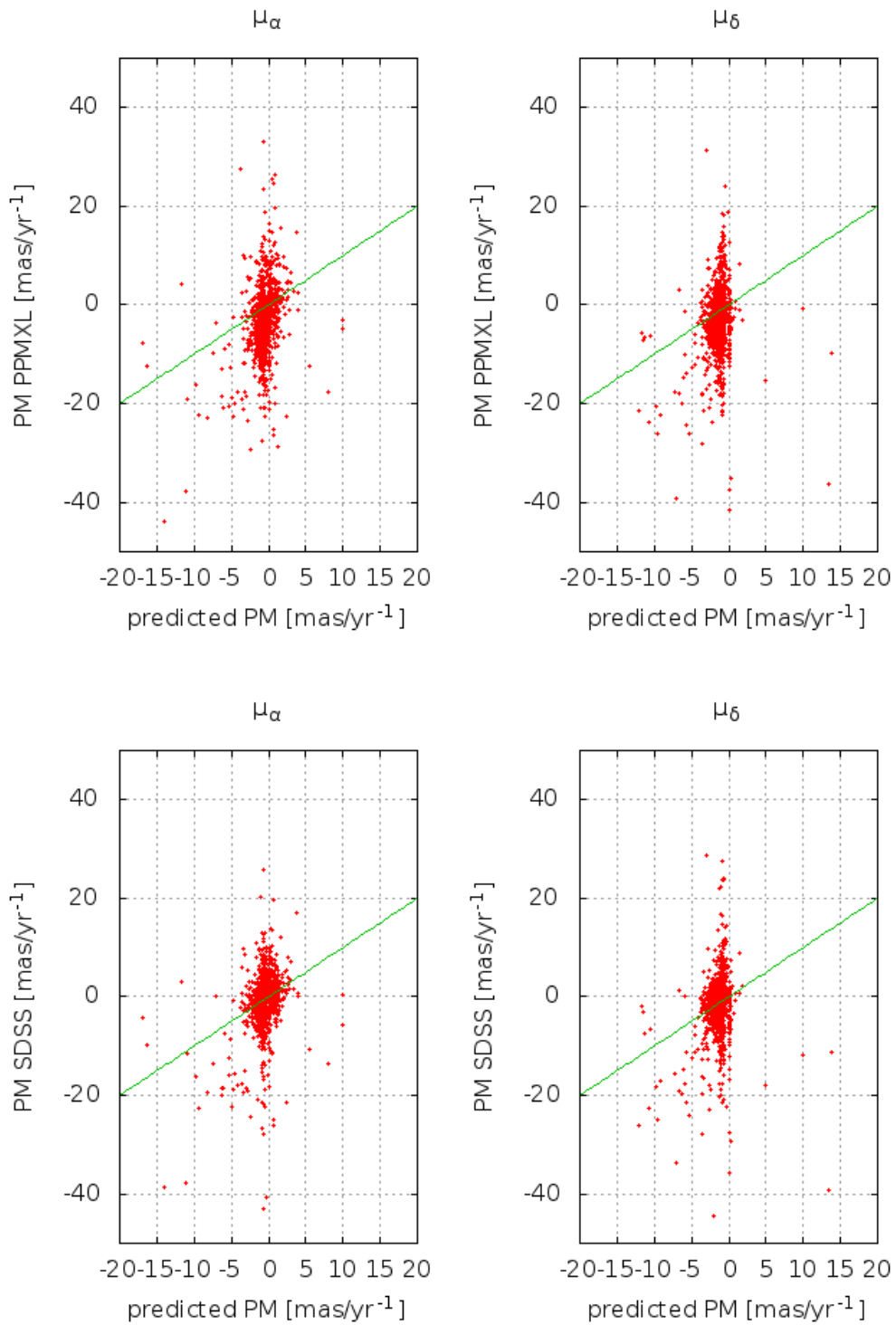
---

[5]http://vo.uni-hd.de/ppmxl

Figure 10: The differences between the predicted proper motion values and the values obtained by PPMXL and SDSS. If the predicted values fit to the measured ones, they should follow the plotteed line. The scattering is too big to make solid statements.

4. Proper motion measurements

The proper motion which was calculated for every object under the condition that it originates from the Galactic center will now be checked against measurements. This will only be done with two objects of the sample, since it is a complicated and time consuming procedure.

4.1. General procedure

Proper motion can be derived by comparing the coordinates of an object measured at different epochs. Comparing, for instance, the coordinates of a star in 1950 and today will proviide a way to derive its angular motion. Therefore, photographic images of the sky from several epochs between 1950 and 2000 will be analyzed and combined with measurements from modern digital surveys (e.g. SDSS). The number of epochs involved should be as large as possible to obtain sufficient statistics. Galaxies are the best reference for the coordinates, since they are too far away to move significantly within the selected time. In the following section, this procedure will be described in detail. Furthermore it will be applied to the candidates SDSS J1537-0150 and SDSS J1641+4723.

4.1.1. Sky survey plates

Sky surveys are great archives for astronomers, which provided a lot of data to the science in the past and even today. One of the key functions is the contribution to post-nova/supernova research and the search for variables with longer periods. Furthermore, they can be used to determine the proper motion of stars, which is done in this work. The most important sky surveys of the 20th century are now presented in a chronographic order in short. Unlike the SDSS, which uses CCD detectors, the surveys were carried out using photographic plates which needed to be digitized to be usable.

- *POSS*: The POSS (Palomar Observatory Sky Survey) was taken in the 50s using the 1.2m Oschin telescope at mount Palomar observatory. It covers the whole northern hemisphere and even some equatorial parts of the sky. A blue and a red plate was taken, both as deep as 22 mag. The depth is unequalled in that time.

- *SERC*: The SERC-Survey was initiated by ESO (European Southern Observatory) in the 80s and ended in 1999. It was planned to be the southern counterpart of the POSS. Moreover, it can be devided into the Southern Sky Atlas (SERC-J), taken at Australia, and the southern Galactic Plane Survey (SERC-R), which was taken at La Silla and many other parts, for example the Equatorial Red Atlas taken with the UK Schmidt telescope.[6]

- *POSS-II*: The POSS-II survey provides a second epoch survey of almost the complete area covered by the former POSS. It started in the 80s. Better photographic plates were used than in the previous survey. Furthermore, an additional plate in the near infrared was taken. POSS-I and especially POSS-II are well described by Reid et al. (1991).

- *2MASS*: The photographic plates obtained by the 2MASS-Survey, (Two Micron All Sky Survey) consist of three different bands in the near infrared. It covers the whole sky, using two 1.3m telescopes at Mt. Hopkins, Arizona, and CTIO, Chile, respectively.

- *SuperCOSMOS*: SuperCOSMOS is not a survey itself, but a project for the digitization of photographic plates to make them available to the public. It also includes photographic data from other surveys.

plates have been digitized until now and are made available in the databases through the internet. This is a major advantage due to a more simple evaluation. Therefore, digitized versions of the plates were used to measure the proper motion. Moreover, these digitized sky surveys provide the basis for todays astrometric catalogues. They have been utilized by different research teams independently to

---

[6]http://galaxymap.org/cgi-bin/gallery.py

create huge catalogues, e.g. by the US Naval Observatory (USNO-B, > 1 billion stars, Monet et al. (2003); UCAC4, 113 million stars, Zacharias et al. (2013)) and the Astronomisches Recheninstitut Heidelberg (PPMXL, 900 million stars, Roeser et al. (2010)).

4.1.2. Measuring the proper motion

To determine the proper motion of a star, it is necessary to measure the position of a star at different epochs. On every digitized plate a reference pixel associated to a specific coordinate in right ascension and declination ist given. Knowing the angular distance per pixel, the position of a star on the plate could be determined. Unfortunately, one pixel may cover about a few arcsec on the sky, depending on the plate scale and quality. Using this reference pixel would therefore lead to a significant systematic error, because the values of the measured proper motion are expected to be in the order of mas yr^{-1}. An absolute reference system would require a net of point sources fixed on the sky. Quasi stellar objects (QSOs) would be the best reference system because they are point-like and very distant. However, QSOs are scarce and too few to form a net. Galaxies are much more abundant and also distant. Using background galaxies as reference points is not the easiest thing to do, since they are often extended irregular light sources and therefore their centers of light can not be measured sufficiently well. However, using many of the most compact galaxies decreases the sensitivity of the resulting value to the position errors of each galaxy and enables a statistical approach. Only the relative distances on the plate - between the galaxies and the star - have been taken into account. The reference pixel was fully ignored. The complete procedure is now described in detail. For this analysis, *MIDAS*[7], a tool for image processing and data reduction published by ESO, was used.

Initially, appropriate galaxies were selected within 15 x 15 arcmin around the selected object, using the SDSS database. Most helpful galaxies are, as described above, on the one hand point-like sources but on the other hand as bright as possible, to be visible even on plates taken with short exposure. This is often a contradiction in itself since - in general - more point-like galaxies are more distant and therefore fainter. Galaxies fulfilling both criteria as well as possible were selected for the measurements. The coordinates found in the SDSS database were used to determine all relative distances between the galaxies and the star. The coordinates of the galaxies serve as a "calibration grid" for all other plates. Finding the specific galaxies on every plate allows to determine the position of a star relative to the galaxies. However, no galaxy is a really point-like source. Therefore, it is difficult to define the correct position of a galaxy on a photo plate. To solve this problem, a Gaussian distribution was fitted to the brightness distribution of each galaxy on every plate. The peak of the Gaussian was associated to the center of the galaxy, from which the relative distances were measured. The width of the Gaussian contributes to the error of the determined proper motion. Subsequently, a *MIDAS*-script compared the relative positions of the selected star to the galaxies on each plate. This was done separately for the movement in right ascension and declination. Plotting the difference of the coordinates of the star relative to the calibration grid over different epochs shows a general trend. The gradient of a linear fit gives the proper motion component of the selected object.

4.2. Proper motion measurement of candidate SDSS J1537-0150

The described procedure was thereafter applied to candidate SDSS J1537-0150. This candidate was chosen because its proper motion was predicted by simulations to be large enough for a measurement of high significance. The values which resulted from the calculations assuming a MS star were as high as -25.9 mas yr^{-1} in right ascension and 13.8 mas yr^{-1} in declination, respectively. The HB option produces (μ_α, μ_δ)=(-8.76 mas yr^{-1}, -1.72 mas yr^{-1}). The fit to determine the true proper motion in both, right ascension and declination, is given in Fig 11. Indeed, the proper motion turned out to be relative high, but the values do not correspond to the values calculated under the assumption that it originates in the Galactic center.
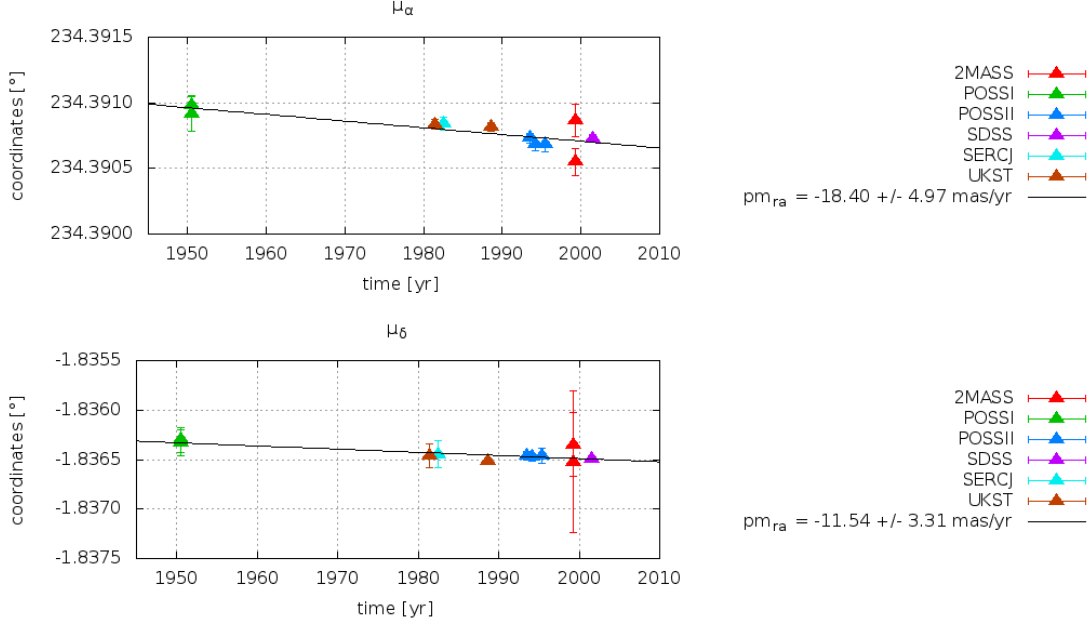
---

[7]http://www.eso.org/sci/software/esomidas/

Figure 11: Proper motion measurement graphs for candidate SDSS J1537-0150. The y-axis shows the change in position over time. The gradient of the linear regression gives the resulting value of the proper motion of the star.

SDSS provides automated proper motion measurements. A third value for the proper motion was found in the PPMXL catalogue. These values were consistent with the measured values in this work and are compared to each other in Tab. 4. The given errors are calculated without any error propagation due to impossible estimation of the errors made during the analysis of the PPMXL and SDSS values.

	PPMXL	**SDSS**	**this work**	**mean value**
pma cos δ	-13.3	-16.4	-18.40 ± 4.97	-16.0 ± 2.1
pmd	-9.8	-11.3	-11.5 ± 3.31	-10.9 ± 0.8

Table 4: Comparison of proper motion values measured in this work and the values measured by PPMXL and SDSS. A heavy evidence for consistency can be seen. The errors of the mean value were calculated without any error propagation due to an impossible estimation of uncertainties of PPMXL and SDSS values - statistics with the three values were applied.

To obtain better initial values - especially to improve the distance estimate - five available SDSS spectra were analyzed. This was done in a third party work by Eva Ziegerer. The obtained values fit well to the assumed ones of the heliocentric closest solution. A comparison is given in Tab. 5. For the assumed values, the solution with the shortest heliocentric distance is given for each of the two options - HB and MS. Fig. 12 shows the position of the star in a $\log T_{eff}$-$\log g$ diagram and additionally some evolutionary tracks and the position of the HB, according to Schaller et al. (1992) and Dorman et al. (1993). The measured values of $\log g$ and T_{eff} are not sufficient to decide whether the star is a HB or a MS star. Mostly, HB stars are very slow rotators with $r_{rot} <$ 15 km s^{-1}, according to Behr (2003). Therefore, detecting a slow or fast rotation of the star can help to clarify its nature. Unfortunately, no significant evidence for rotation could be found. Due to the moderate resolution, $v_{rot} \sim 100$ km s^{-1} means just noise in the spectrum. This limit was slightly exceeded by the value of ~ 125 km s^{-1}. Nevertheless, the quality of the spectrum was not sufficient to claim significant rotation. Moreover, HB stars with the measured T_{eff} have expected $\log g$ values between 2.55 and 2.95, according to the stellar structure model grids. The error of the
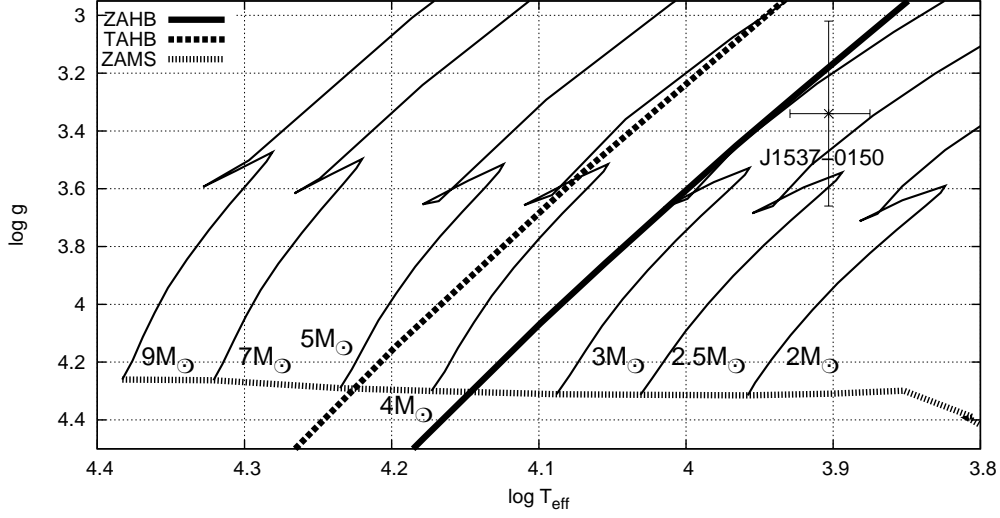
Figure 12: Position of candidate J1537-0150 according to a spectral analysis done by Eva Ziegerer in a $\log T_{eff}$-$\log$ g diagram with evolutionary tracks for MS stars, derived by Schaller et al. (1992) and the locations of ZAHB (Zero Age Horizontal Branch), TAHB (Terminal Age Horizontal Branch) and ZAMS (Zero Age Main Sequence), derived by Dorman et al. (1993). Solar metallicity is assumed.

atmospheric parameters is sufficiently large to make two options possible: If $\log g$ is at the upper edge of the errorbar, SDSS J1537-0150 could be a MS star at the end of his H-burning phase. On the other hand, if $\log g$ is at the lower edge of the errorbar, the star could be a HB star.

However, trajectory simulations showed that a MS option is too distant to originate in the Galactic disk with the measured values. As the ZAHB solution fits best to the spectrum in log g (see Fig. 12), this option is preferred, and therefore given as HB solution in Tab. 5. All in all, the discrepancies are in an acceptable order of magnitude and are presumably based on the insufficient resolution of the spectra. The star must be identified as an HB star. This is consistent considering the 1 σ errorbars. To check this decision, spectra with higher resolution are needed.

	assumed 3M$_\odot$	**HB**	**SDSS spectra**
T_{eff} [K]	7000	7000	8000 ± 500
$\log g$	3.65	2.95	3.34 ± 0.32
v_{rad} [km s^{-1}]	-14.3 ± 1.8 k	-14.3 ± 1.8	-18.5 ± 3.7
d_{helio} [kpc]	7.47 ± 3.35	7.16 ± 3.21	HB: 6.00 ± 2.47 / MS: 13.29 ± 5.43

Table 5: Comparison of assumed and measured stellar parameters of candidate SDSS J1537-0150. The solutions with the shortest heliocentric distance are given, T_{eff} and $\log g$ values are given without an error due to the applied method, described in Sec. 2.1.3. The measured data was obtained by an analysis of five SDSS spectra. The difference in v_{rad} is due to the different spectral analysis by SDSS and Eva Ziegerer, respectively.

As a note it should be mentioned that Tab. 5 is an important hint that the chosen parameter configurations in Sec. 2.1.3 were consistent and proves the method applied.
Calculating the trajectory back in time using the measured values for the proper motion shows that the star hits the Galactic disk at a distance of about 6 kpc to the Galactic center. Fig. 13 shows the significant difference between the measured trajectory and the trajectory calculated under the assumption that the star originates in the Galactic center. To study the effect of the errors on the input parameters a Monte Carlo analysis was applied (see right part of Fig 13). In this analysis, every input parameter is varied randomly within a Gaussian distribution with a width of 1 σ. Ten thousand trajectories are calculated this way, with slightly different initial conditions. The result
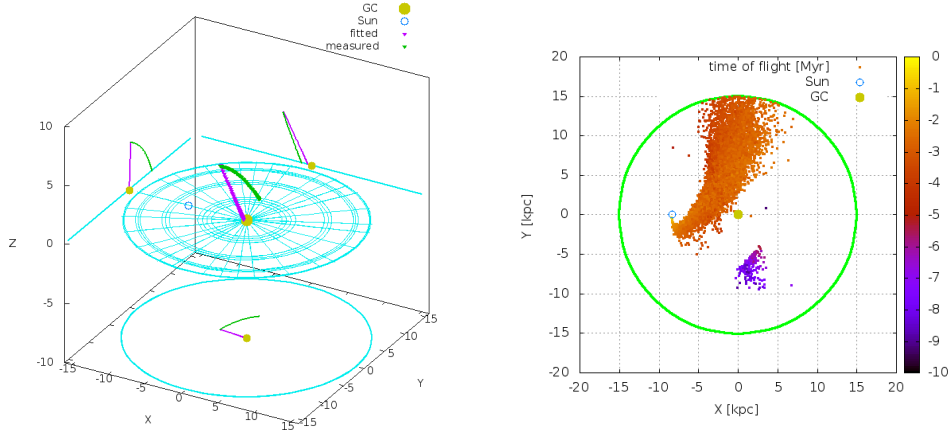
Figure 13: Comparison of calculated and measured trajectory of candidate SDSS J1537-0150 (left). The origin in the Galactic center can be ruled out considering a 1 σ Monte-Carlo simulation (right).

of this calculation shows, that an origin in the Galactic center can indeed be ruled out, at least at the 1 σ level. In Tab. 6 typical velocities of the calculated trajectories and, in addition, the time of flight from the Galactic disk to the current position are given. Note, that v_{ej} is the velocity at the time of ejection in the Galactic disk without the intrinsic v_{rot} of a star on an orbit around the center of the Milky Way. This velocity therefore describes the acceleration which is needed to kick the star out of the Galactic disk to its current position.

	v_{grf} **[km s^{-1}]**	v_{esc} **[km s^{-1}]**	v_{ej} **[km s^{-1}]**	t_{flight} **[Myr]**
ZAHB (fitted to GC)	183.4	572.9	729.3	17.34
spectra(HB) (real)	381.0	575.6	152.0	17.64

Table 6: Comparison of typical velocities of candidate SDSS J1537-0150. v_{grf} is the current Galactic rest-frame velocity of the object, v_{esc} is the local escape velocity at the current position of the star. v_{ej} gives the velocity at the time of ejection in the Galactic disk, neglecting external acceleration via the Galactic rotation v_{rot} (240 km s^{-1} at the calculated distance of 5.8 kpc to the Galactic center). The expected proper motion of the fitted solution is $(\mu_\alpha, \mu_\delta) = $ (-8.8,-1.7), its distance would be 7.16 $\pm$ 3.21 kpc.

Both, the assumed values for calculation and the measured values, indicate a time of flight which is fully consistent with the lifetime of a HB star. The spectral analysis shows, that the star is bound to the Galaxy and was ejected at 152.0 km s^{-1}, neglecting external acceleration via the Galactic rotation v_{rot}, which is 242.5 km s^{-1} at the place of ejection. The given values assume ejection in the direction of the rotation of the Milky Way. Its current Galactic rest-frame velocity is 381.0 km s^{-1}. This exceeds the 275 km s^{-1} limit set by Brown et al. (2007) by far. Therefore it can be associated to the category of bound hypervelocity stars mentioned in Sec. 1.1.

4.3. Comparison of different potential models

Working with potential models of the Milky Way and calculating trajectories implies that a well understood potential model is needed. The model used in this work was already described in Sec. 1.4 in detail and two more potential models were mentioned. The consistency of all three models will now be checked using the measured values of candidate SDSS J1537-0150 and calculating its trajectory in each potential. This will furthermore answer the questions if using the potential

model of Allen & Santillan (1991) was an adequate choice and how much the results depend on the choice of the potential model.

4.3.1. Three different potential models

The model used for all calculations in this work ("model *I*") was already described in Sec. 1.4 in detail. The free parameters of the model were calibrated using the rotation curve of the Milky Way. Another analytical potential model was studied and calibrated by Wilkinson & Evans (1999) and Sakamoto et al. (2003) ("model *II*"). The only difference between the two models is the shape and the mass of the dark matter halo around the Galaxy. The terms of the potential which describe the disk and the bulge are exactly the same. A calibration of the halo potential was made using halo objects, such as globular clusters, satellite galaxies and HB stars.

The third potential model ("model *III*") has the same structure - the difference is again just found in the halo term - and was described by Navarro et al. (1997). This potential was calibrated using cosmological simulations.

Comparing these models is a matter of consequences. All models were calibrated using different approaches. Congruence would therefore be evidence for a well designed description of the Milky Way potential.

Note that mass models and potentials are not the main part of this work. Thus, again the reference to Irrgang et al. (2013) is warmly recommended for readers who hold interest for these potential models.

4.3.2. Comparing results in different potential models

The trajectory of candidate SDSS J1537-0150 is now calculated again in every potential model considered above. The parameters obtained from the spectrum of the candidate were used. The point of ejection in the Galactic disk as well as the velocity at the time of ejection and the time of flight to its present position serve as indicators for the consistency of the resulting trajectories.
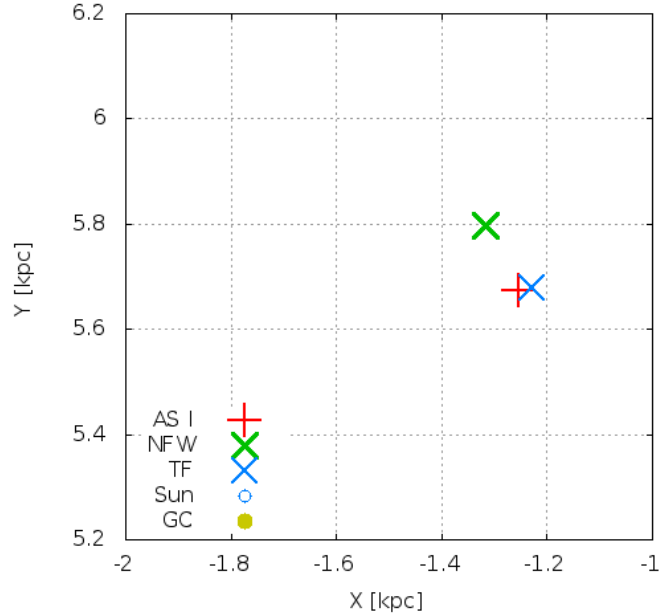

Figure 14: Comparison of places of ejection in the Galactic disk of candidate SDSS J1537-0150 in three different Milky Way potential models, marked with different crosses. A section of the Galactic disk plane is shown. The potential model used in this work ("model *I*", Allen & Santillan (1991)) yields a place of ejection which lies almost between the place produced by other potential models.

The places of ejection from the Galactic disk are marked in a top-view plot of a section of the Galactic disk in Fig. 14. Comparing the marked positions indicates the consistency of all three potentials. Note, that the place of ejection calculated with potential model I is located almost between the ones calculated using other potential models. Additionally, Tab. 7 summarizes the key parameters of the trajectories. The resulting trajectories are almost equal. The values obtained using the potential model I are close to the other values. This is another important hint, that the chosen potential provides "mean" trajectories. Nevertheless, both other potentials are also in very good agreement with potential I, the differences in v_{ej} and in the time of flight are negligible. However, the local escape velocity v_{esc} at the current position of the star depends strongly on the choice of the potential model. This is a direct consequence of the different treatment of the dark matter halo in the models. Although the potentials of the Galactic disk and the bulge are the same in each model, the depth of the potential at the current position of the star is dominated by the dark matter halo term. Therefore, a strong influence of the chosen model on v_{esc} is expected - and indeed observed.

potential model	v_{ej} [km s^{-1}]	v_{esc} [km s^{-1}]	time of flight [Myr]
I	152.0	572.9	17.64
II	152.3	547.7	17.63
III	152.9	666.0	17.75

Table 7: Typical velocities and time of flight of candidate SDSS J1537-0150 in three different Milky Way potential models. The velocity at the time of ejection from the Galactic disc v_{ej} is given, neglecting external acceleration via the Galactic rotation v_{rot}. Consistency can be seen in v_{ej} and in the time of flight. The large differences of the local escape velocity can be explained by the different shape and mass of the dark matter halo in each potential.

All in all, the three models are consistent among themselves. Differences, for example seen in the local escape velocity, become significant on larger distance scales, but in such calculations other galaxies such as the Magellanic clouds and Andromeda would also have a significant influence on the trajectory. Therefore, the model could not be used on these scales anyway. The chosen potential model I in this work provides mean trajectories and was therefore a decent choice. However, by only calculating one single trajectory in every potential model, one is not able to make general statements about the potential models. Especially for complex trajectories a divergence of the solutions is expected. Nevertheless, the test given in this section shows, that all potential models can cope with moderate problems.

4.4. Proper motion measurement of candidate SDSS J1641+4723 (HVS 17)

In the course of this project a spectroscopic analysis of HVS 17 (SDSS J164156.39+472346.1) was published by Brown et al. (2013) using high resolution spectroscopy (Keck:II-Telecope). Most important results from the spectral analysis by Brown et al. (2013) are summarized in Tab. 8. Since the star was also in the sample studied in this work, the proper motion was measured (see Fig. 15).

	Brown et al. (2013)	This work
T_{eff} [K]	12350 ± 290	13000
$\log g$	3.80 ± 0.086	3.85 (MS) / 4.15 (HB)
dist [kpc]	48.5 ± 4.6	50 (MS) / 14 (HB)

Table 8: Results of the spectral analysis done by Brown et al. (2013) of HVS 17 compared to the parameters derived in this work.

Fig. 16 shows the resulting position in a $\log T_{eff}$-$\log g$ diagramm. The star is found in an area in which it can not clearly be identified as a HB and MS star, respectively. Brown et al. (2013) concluded that HVS 17 is a 3.91 ± 0.09 M$_\odot$ MS star, because it has solar metal abundance and in
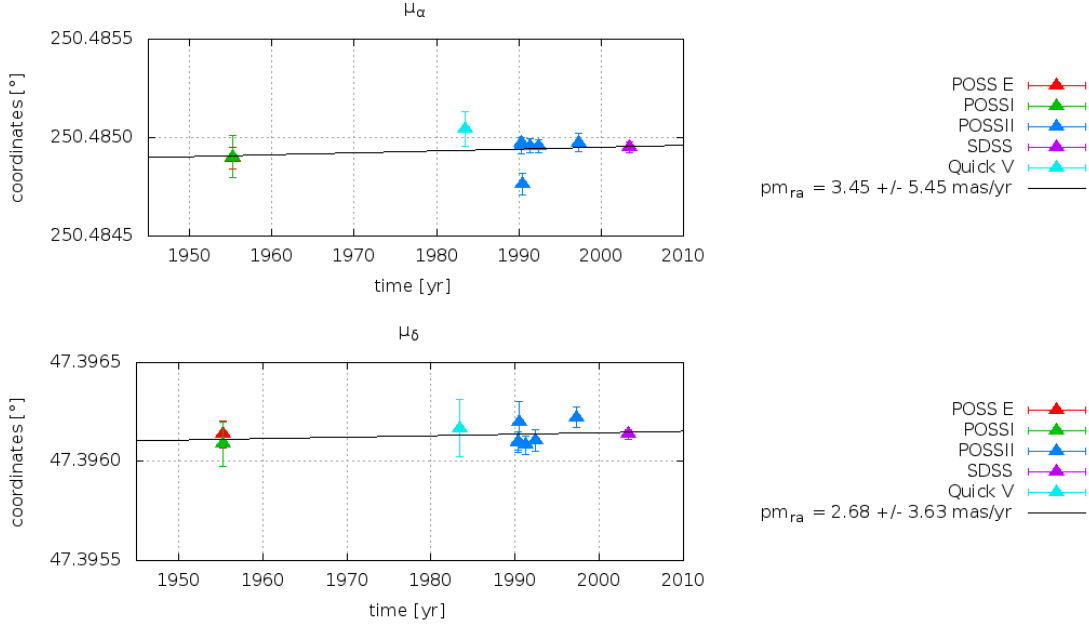
Figure 15: Proper motion measurement graphs for candidate SDSS J1641+4723. The y-axis shows the change in position over time. The gradient of the linear regression gives the resulting value for the proper motion of the star.

fact not low metal abundance, as expected for a HB star. Furthermore, the star is a fast rotator with $v \sin i = 68.7 \pm 5.4$ km s^{-1}. Typical rotation velocities of HB stars are < 15 km s^{-1} (Behr, 2003). Therefore, the HB option was ruled out by Brown et al. (2013).
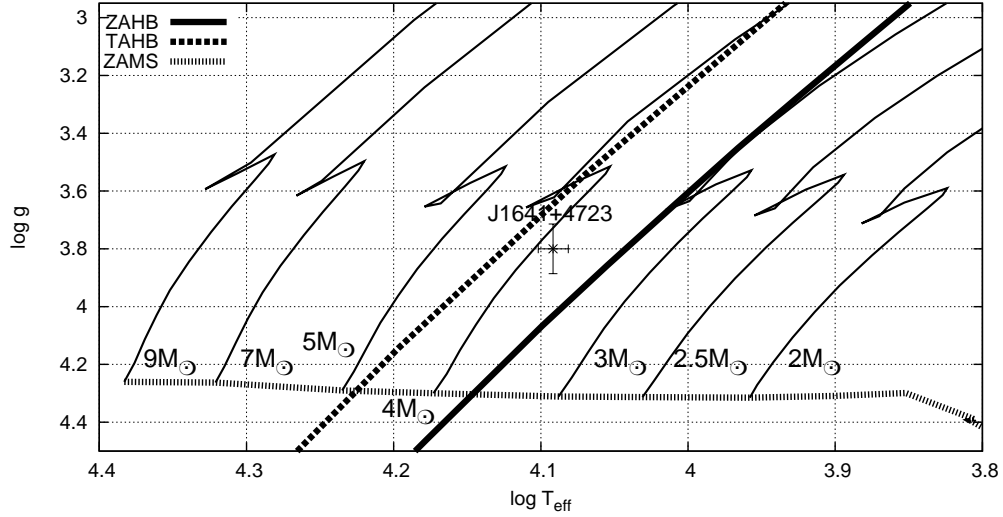
Figure 16: Position of candidate J1641+4723 according to a spectral analysis by Brown et al. (2013) in a log T_{eff}-log g diagramm with evolutionary tracks for MS stars, derived by Schaller et al. (1992) and the locations of ZAHB (Zero Age Horizontal Branch), TAHB (Terminal Age Horizontal Branch) and ZAMS (Zero Age Main Sequence), derived by Dorman et al. (1993). Solar metallicity is assumed.

Furthermore, Brown et al. (2013) calculated expected proper motion values for the star to originate in the Galactic center. In Tab. 8 these values are compared to the ones computed in this work.

Both options - HB and MS - are listed. Furthermore, the measured values are given for comparison again. Considering the errors, the measured values indeed fit to the ones predicted by Brown et al. (2013) under the assumption that the star originates in the Galatic center. Moreover, the predicted values fit to the values computed in this work, which shows consistency. In fact, the predicted proper motion for the HB option to originate in the Galactic center does not fit to the measured values.

Unfortunately, the uncertainties of the measured values are too large calculate trajectories with sufficient precision to make statements about the origin of the star. At distances of about 50 kpc small changes in proper motion have large effect on the trajectory. Therefore no place in the entire Milky Way could be ruled out as a possible origin of HVS 17. Even considereing the HB solution no statement about the origin was possible.

Nevertheless, assuming a Galactic center origin, the star shows a v_{grf} of 444.3 km s^{-1} in the potential model used. This exceeds the model's local escape velocity at the star's position by about 100 km s^{-1}, which leads to an unbound orbit. The star was ejected at 802 km s^{-1} and needs 91.30 Myr to arrive at its present position. This is fully consistent with the lifetime of 153 ± 9 Myr derived by Brown et al. (2013).

5. Conclusion and Outlook

The aim of this work was to find new hypervelocity stars considering the full 3D velocity and not only the radial component. Simulations were made to derive expectation values of proper motion for each star in a sample of 1300 objects under the assumption that they originate in the Galactic center. Comparing the calculated proper motion values to the values obtained by SDSS and PPMXL databases shows that there is no significant evidence for fast halo stars to be accelerated in the Galactic center. The proper motion of the candidate SDSS J1537-0150 was measured in this work. The results are consistent with the values measured by SDSS and PPMXL, but do not fit to the values predicted by the simulations. Tracing the trajectory back in time shows, that the star was ejected from the Galactic disk at a distance of about 6 kpc to the Galactic center with a velocity of 152 km s^{-1}, neglecting external acceleration via the Galactic rotation v_{rot} and considering ejection in the direction of rotation of the Milky Way. An origin in the Galactic center could be ruled out. The target could be identified as a bound hypervelocity star, exceeding 275 km s^{-1} (which is the classification criterion as defined by Brown et al. (2007)) due do its high Galactic rest-frame velocity (381.0 km s^{-1}). To clarify the nature SDSS J1537-0150, high resolution spectra are needed to derive rotation and metallicity, and therefore decide between MS and HB option with more certainty.

Furthermore HVS 17, which was in the sample studied in this work, was revisited. The data obtained by Brown et al. (2013) in a spectral analysis using the Keck:II telescope and prediction about the proper motion fit well to the data obtained by the temperature selection applied in this work. The star is likely to be a 3 M$_\odot$ MS star.

Three different analytical potential models of the Milky Way were also checked for consist results. One of them was studied by Allen & Santillan (1991) and Irrgang et al. (2013) and used for orbit calculations in this work. The two other potential models were applied to calculate the trajectory of candidate SDSS J1537-0150 again. Indeed, all potential models produce almost equivalent trajectories, which shows, that the potential of the entire Milky Way is well understood on distance scales of a few up to a few tens of kpc from the Galactic center, but the local escape velocity strongly depends on the assumed halo mass.

According to Brown (2008), the expected proper motion values for a HVS at a distance of about 50 kpc are a few tenths of an arcsec per year, if a star originates in the Galactic center. Indeed, no HVS was found because of its high proper motion yet. Therefore, observing HVS with high proper motion would challenge the Hills paradigm and may furthermore be a hint on the unsolved question of the acceleration mechanism. In the future, surveys providing accurate astrometry will become available. Especially *Gaia*[8] is a promising project which is planned to provide proper motion measurements with μas yr^{-1} accuracy and additional μas-parallax measurements, which are independent from the stellar evolution models. This will simplify the procedure of proper motion measurements, and automated high quality measurements will be possible. The ability to search for stars with high proper motion in a large sample of objects could provide a long list of new HVS. Subsequently, statistical methods can be applied to the sample of HVS and significant results can solve the question about their origin. Furthermore, extreme halo objects provide much information about the mass of the Milky Way and especially the mass and the shape of the dark matter halo. Hypervelocity stars therefore remain a promising field for future investigations.

---

[8]http://sci.esa.int/gaia/

A. List of the most promising candidates

ra	dec	m_v	μ_α(c)	μ_δ(c)	μ_α(S)	μ_δ(S)	v_{grf}	v_{esc}	b/ub
15 21 33.47	00 46 53.49	16.27	-3.6	-3.6	6.0	-28.0	12.4	542.1	b
15 21 33.47	00 46 53.49	16.27	-2.9	-3.2	6.0	-28.0	4.3	527.7	b
13 52 37.98	-01 32 29.62	15.08	3.4	-11.5	-21.3	-22.7	398.4	539.1	b
15 37 33.77	-01 50 11.38	15.08	-25.9	13.8	-16.4	-11.3	824.9	575.4	ub
15 37 33.77	-01 50 11.38	15.08	-8.8	-1.7	-16.4	-11.3	183.4	572.8	b
15 42 15.66	25 22 01.05	15.78	-6.4	0.3	-18.5	7.3	211.7	532.1	b
16 29 59.70	16 03 56.39	14.81	-10.6	8.7	3.1	-39.2	455.5	563.6	b
14 36 29.67	00 45 19.37	15.34	0.7	-11.4	-26.1	-3.1	269.3	553.3	b
20 46 05.95	-06 17 16.42	15.17	-7.4	-9.2	-13.5	-17.2	214.0	567.7	b
13 46 22.70	64 20 55.37	15.23	-9.4	-0.8	-22.6	-3.4	191.1	507.1	b
17 20 13.59	27 41 18.50	14.84	-0.4	-27.9	-22.3	-6.8	574.7	557.4	ub
14 36 15.59	51 55 21.30	14.76	-11.2	1.5	-37.8	8.9	211.1	523.7	b
15 54 25.98	06 46 31.49	14.97	-26.7	22.8	-23.2	7.3	939.4	570.1	ub
16 42 39.30	20 46 54.99	15.56	-0.6	-11.6	-4.8	-1.8	299.1	555.8	b
16 42 39.30	20 46 54.99	15.56	-1.5	-6.5	-4.8	-1.8	199.3	542.4	b
12 21 27.64	35 05 12.95	14.87	-10.9	-5.8	-11.5	-21.4	175.8	515.3	b
10 22 36.78	25 18 40.62	14.72	-0.5	-12.0	2.0	-26.0	161.0	507.6	b
10 07 17.68	22 17 33.04	14.88	-9.8	-7.0	-16.3	-33.7	300.3	504.1	b
01 36 55.90	24 25 45.97	15.86	10.0	-1.5	-5.6	-5.4	495.2	482.5	ub
14 56 04.70	00 49 05.50	15.37	-0.5	-8.7	-13.5	-9.8	230.8	552.5	b
12 05 03.24	48 04 25.75	15.57	-16.2	-2.6	-9.8	-17.8	489.3	506.1	b
00 28 10.33	21 58 09.68	17.42	2.9	-0.9	3.5	-1.8	294.7	436.3	b
13 37 57.40	00 56 47.25	17.83	-1.0	-3.2	8.5	0.8	211.8	475.2	b
11 33 12.13	01 08 24.87	17.89	-3.6	-1.2	-1.1	0.4	452.3	451.0	b/ub
12 54 05.94	02 01 16.28	17.69	-3.4	-1.9	-2.9	-1.4	199.8	472.0	b
15 22 09.70	02 08 24.55	17.79	-1.0	-3.6	0.0	-2.8	239.9	498.6	b
13 04 07.10	43 11 08.74	17.65	-3.6	-1.7	0.7	-3.3	259.7	457.2	b
02 16 21.23	00 07 58.54	17.37	4.0	-2.0	0.6	-7.3	245.6	452.5	b
14 24 16.88	-01 43 35.03	16.52	-8.2	-2.5	-6.9	-0.6	182.0	543.2	b
12 37 53.23	43 31 53.78	16.52	-2.2	-5.9	-2.3	0.1	243.9	495.1	b
08 28 30.33	16 57 46.48	16.39	-1.7	-5.8	-3.8	1.4	181.6	480.1	b
17 19 47.87	59 16 04.33	16.8	-4.0	8.2	-3.7	2.0	446.9	506.5	b
16 12 53.21	06 05 38.78	15.46	4.0	-10.1	1.9	-1.3	331.7	573.7	b
16 12 53.21	06 05 38.78	15.46	-457.9	833.3	1.9	-1.3	25293.8	575.3	ub
16 12 53.21	06 05 38.78	15.46	-30.5	36.8	1.9	-1.3	1664.4	572.6	ub
16 05 33.50	36 49 40.19	15.4	-11.0	3.7	-9.1	-4.2	204.7	544.3	b
22 30 28.66	00 07 31.49	16.47	-3.5	-7.4	-1.1	-8.5	246.2	526.9	b
10 05 07.92	35 13 57.51	16.78	-3.5	-6.0	7.3	-4.4	143.3	481.0	b
13 19 16.16	-01 14 05.03	16.43	-17.0	0.3	-4.2	-6.7	420.9	535.5	b
10 13 39.56	44 57 34.31	20.42	10.0	10.0	2867.9	0.6	-11.9	356.1	ub
16 39 36.03	34 32 30.45	15.14	0.0	-26.5	-2.9	-6.2	362.8	550.9	b
14 43 01.69	51 44 10.34	16.08	-5.9	-4.5	-7.4	-11.3	48.8	522.0	b
12 04 08.22	15 36 09.70	16.4	-5.2	-7.3	-8.7	-15.7	31.4	513.3	b
11 31 49.30	34 41 00.93	16.06	-1.5	-10.6	-4.3	-6.6	162.5	509.5	b

Table 9: List of the most promising candidates. Proper motion columns marked as (c) were calculated in this work under the assumption that the trajectory of the star originates in the Galactic center. Columns marked as (S) were obtained by the SDSS using an automated algorithm. The last column indicates whether a star is bound (b) or unbound (ub) to the Milky Way.

ra	dec	teff(Photo.bin)	teff(spek)	logg(calc)	logg(spek)
15 21 33.47	00 46 53.49	7000	11912	3.65	3.77
15 21 33.47	00 46 53.49	7000	11912	2.95	3.77
13 52 37.98	-01 32 29.62	7000	11223	3.65	3.43
15 37 33.77	-01 50 11.38	7000	8025	3.65	3.34
15 37 33.77	-01 50 11.38	7000	8025	2.95	3.34
15 42 15.66	25 22 01.05	7000	11282	3.65	3.63
16 29 59.70	16 03 56.39	7000	11162	3.65	3.26
14 36 29.67	00 45 19.37	8000	11777	3.95	4.03
20 46 05.95	-06 17 16.42	8000	8934	3.95	4.20
13 46 22.70	64 20 55.37	8000	11001	3.95	4.14
17 20 13.59	27 41 18.50	8000	9061	3.95	4.10
14 36 15.59	51 55 21.30	8000	10098	3.95	4.38
15 54 25.98	06 46 31.49	8000	10281	3.95	4.01
12 21 27.64	35 05 12.95	8000	10810	3.95	3.86
10 22 36.78	25 18 40.62	8000	11427	3.95	3.79
10 07 17.68	22 17 33.04	8000	14850	3.95	4.60
14 56 04.70	00 49 05.50	9000	9065	4.30	3.10
12 05 03.24	48 04 25.75	9000	9340	4.30	3.20
13 37 57.40	00 56 47.25	12000	12361	4.00	3.51
11 33 12.13	01 08 24.87	12000	14969	4.00	3.19
02 16 21.23	00 07 58.54	12000	12609	4.00	3.47
14 24 16.88	-01 43 35.03	13000	13583	4.15	3.45
17 19 47.87	59 16 04.33	14000	16222	4.30	4.15
22 30 28.66	00 07 31.49	14000	16493	4.30	4.11
13 19 16.16	-01 14 05.03	15000	15593	4.45	4.14
10 13 39.56	44 57 34.31	15000	18244	4.45	3.89

Table 10: Comparison of chosen T_{eff} and $\log g$ values due to the temperature analysis and the values obtained by analyzing a SDSS spectrum. This list covers all targets from Tab. 9, of which spectra were available in the SDSS database.

B. Comparison of proper motion data provided by SIMBAD and SDSS
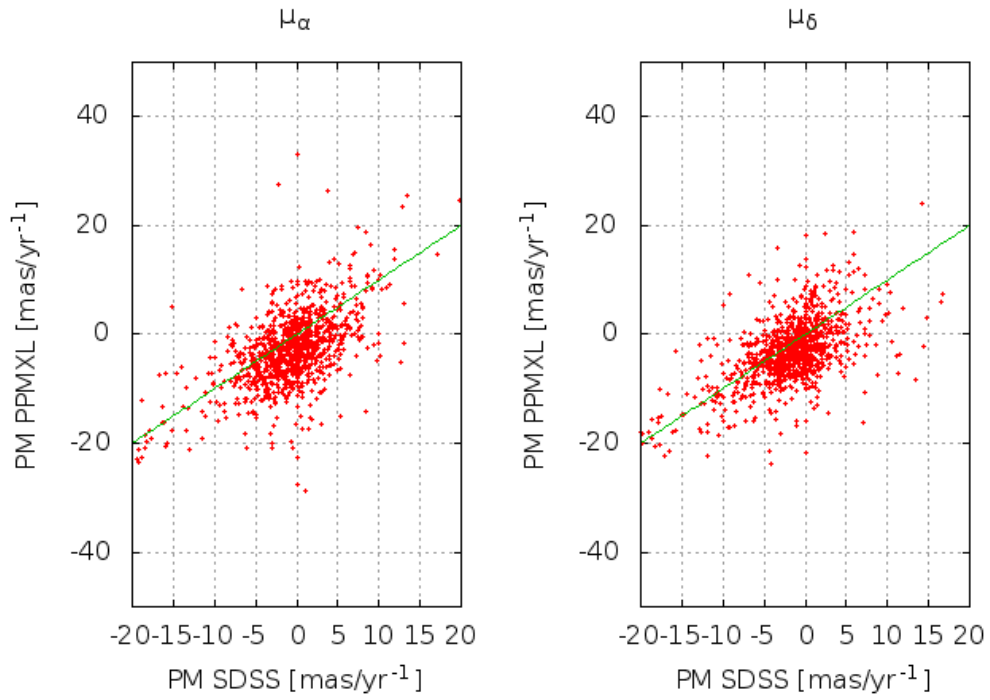
Figure 17: Adapted from Sec. 3.2.2, PPMXL and SDSS data are compared by plotting the values in each, right ascension and declination. Lacks of consistency can be seen. The expected correlation is marked as the green line.

List of Figures

List of Tables

References

Abadi M.G., Navarro J.F., Steinmetz M., 2009, ApJ691, L63

Allen C., Santillan A., 1991, Rev. Mexicana Astron. Astrofis.22, 255

Behr B.B., 2003, ApJS149, 101

Brown W.R., 2008, ArXiv e-prints

Brown W.R., Cohen J.G., Geller M.J., Kenyon S.J., 2013, ArXiv e-prints

Brown W.R., Geller M.J., Kenyon S.J., 2012, ApJ751, 55

Brown W.R., Geller M.J., Kenyon S.J., Kurtz M.J., 2005, ApJ622, L33

Brown W.R., Geller M.J., Kenyon S.J., et al., 2007, ApJ660, 311

Castelli F., Kurucz R.L., 2004, ArXiv Astrophysics e-prints

Dorman B., Rood R.T., O'Connell R.W., 1993, ApJ419, 596

Edelmann H., Napiwotzki R., Heber U., et al., 2005, ApJ634, L181

Geier S., Hirsch H., Tillich A., et al., 2011, A&A530, A28

Geier S., Marsh T.R., Wang B., et al., 2013, A&A554, A54

Genzel R., Eisenhauer F., Gillessen S., 2010, Reviews of Modern Physics 82, 3121

Gualandris A., Portegies Zwart S., 2007, MNRAS376, L29

Heber U., Edelmann H., Napiwotzki R., et al., 2008, A&A483, L21

Hills J.G., 1988, Nature331, 687

Hirsch H.A., Heber U., O'Toole S.J., Bresolin F., 2005, A&A444, L61

Irrgang A., Przybilla N., Heber U., et al., 2010, ApJ711, 138

Irrgang A., Wilcox B., Tucker E., Schiefelbein L., 2013, A&A549, A137

Jester S., Schneider D.P., Richards G.T., et al., 2005, AJ130, 873

Kim S.S., Lee M.G., 2007, PASP119, 1449

Kurucz R.L., 1992, In: Barbuy B., Renzini A. (eds.) The Stellar Populations of Galaxies, Vol. 149. IAU Symposium, p. 225

Monet D.G., Levine S.E., Canzian B., et al., 2003, AJ125, 984

Navarro J.F., Frenk C.S., White S.D.M., 1997, ApJ490, 493

Reid I.N., Brewer C., Brucato R.J., et al., 1991, PASP103, 661

Roeser S., Demleitner M., Schilbach E., 2010, AJ139, 2440

Sakamoto T., Chiba M., Beers T.C., 2003, A&A397, 899

Schaller G., Schaerer D., Meynet G., Maeder A., 1992, A&AS96, 269

Schödel R., 2011, In: Zapatero Osorio M.R., Gorgas J., Maíz Apellániz J., Pardo J.R., Gil de Paz A. (eds.) Highlights of Spanish Astrophysics VI., p.36

Smith J.A., Tucker D.L., Kent S., et al., 2002, AJ123, 2121

Tillich A., Heber U., Geier S., et al., 2011, A&A527, A137

Wilkinson M.I., Evans N.W., 1999, MNRAS310, 645

Yu Q., Tremaine S., 2003, ApJ599, 1129

Zacharias N., Finch C.T., Girard T.M., et al., 2013, AJ145, 44

Zhang F., Lu Y., Yu Q., 2013, ApJ768, 153

Acknowledgements

Erklärung

Hiermit erkläre ich, diese Bachelorarbeit in Eigenarbeit angefertigt zu haben, sofern nicht explizit in Text oder Referenzen vermerkt. Diese Arbeit ist der Universität Erlangen-Nürnberg als Vorraussetzung für den Erhalt des Abschlusses *Bachelor of Science* vorgelegt worden. Ich erkläre, dass diese Arbeit weder partiell noch als Ganzes für den Erhalt eines anderweitigen Abschlusses verwendet wurde und wird.

<table>
<tr><td>Erlangen, 17.09.2013</td><td></td><td></td></tr>
<tr><td>Ort, Datum</td><td></td><td>Simon Kreuzer</td></tr>
</table>